ABSTRACT

Title of dissertation: PHOTON PAIR PRODUCTION
FROM A HOT ATOMIC ENSEMBLE
IN THE DIAMOND CONFIGURATION

Richard Thomas Willis, Doctor of Philosophy, 2009

Dissertation directed by: Professor Steven Rolston
Department of Physics

This thesis discusses four-wave mixing (4WM) in a warm ensemble of rubidium using the diamond configuration level structure. Both classical 4WM and non-classical photon-pair production are investigated.

Quantum information science has spawned a great amount of experimental work on the interaction of light with collective modes of excitation in atomic ensembles. Plans to build quantum networks and quantum repeaters with atom ensembles take advantage of nonlinear interactions to produce and store non-classical states of light. These technologies will require photon sources that not only generate non-classical light, but also resonant, narrow band light. Here we investigate a system which could be used as such a source.

We take advantage of the 4WM interaction in a warm ensemble of Rubidium atoms. Our scheme utilizes the diamond energy level configuration which, in rubidium, allows for correlated pairs at telecommunications wavelengths. We start by examining the properties of classical 4WM in the system. We measure the reso-

nance structure and see that it can be understood in terms of velocity class selective resonant enhancement and power splitting effects. The efficiency of the process is low and limited by linear absorption of the pumps. Our observations agree with a semi-classical Maxwell-Bloch theoretical treatment.

Next we observe pair generation by spontaneous 4WM from the warm ensemble. The temporal profile of the cross-correlation function (CCF) for the photons depends on pump-laser power and detuning. This allows us to produce biphotons with controllable spectra. A simple quantum optical theoretical treatment based on linear filtering gives qualitative agreement with the data.

We show that the photon pairs are polarization entangled, clearly violating Bell's Inequality. A perturbative quantum optical treatment predicts the polarization state of the pairs and agrees with our measurements. We analyze the photon statistics of the source and find the largest violation of the two beam Cauchy-Schwarz inequality from a warm atomic source yet. We cast the system as a heralded single photon source at telecommunications wavelengths and see that it is competitive with other systems in terms of spectral brightness.

PHOTON PAIR PRODUCTION FROM A HOT ATOMIC ENSEMBLE IN THE DIAMOND CONFIGURATION

by

Richard Thomas Willis

Dissertation submitted to the Faculty of the Graduate School of the
University of Maryland, College Park in partial fulfillment
of the requirements for the degree of
Doctor of Philosophy
2009

Advisory Committee:
Professor Steven Rolston, Chair/Advisor
Professor Luis Orozco
Dr. Charles Clark
Professor Mario Dagenais
Dr. Paul Lett

Dedication

This work is dedicated to my mother.

Acknowledgments

I would like to thank both of my advisors, Luis Orozco and Steve Rolston, for teaching me how to do experimental physics and for giving me the opportunity to work for them. I want to express my gratitude to my labmate, Francisco Elohim Becerra-Chavez, and all of the other students in both the Orozco and Rolston groups for all of their help and camaraderie.

I would not have been able to finish this ordeal without the help of several key people. They are, in the order that I met them, my mother Kathryn Willis, my brother Jonathan Willis, and my girlfriend Tracy Moore. Thank you very much for everything that you have done for me. I love you all.

Table of Contents

List of Figures

Chapter 1

Introduction to Correlated Photons From Atomic Ensembles

1.1 Introduction: The Basics of the System

This thesis is concerned with the experimental demonstration of a quantum mechanically correlated photon pair source. The generation medium used here is a laser pumped vapor cell of warm rubidium. The scheme takes advantage of a spontaneous four wave-mixing (4WM) interaction in the atoms to create photon pairs that are correlated in direction, frequency, polarization, and time. Correlated photon pairs have numerous applications and the main motivation for this work is the future applications of this source for quantum communication (see section 1.2).

We work with a warm atomic ensemble of ^{85}Rb and apply two pump beams to the atomic vapor. Figure 1.1a shows the basic geometry of the generation scheme. The two pump lasers are at 795 nm and 1324 nm and propagate in directions defined by k-vectors $\vec{k}_1$ and $\vec{k}_2$, respectively. Due to the 4WM interaction, photon pairs are generated at 1367 nm and 780 nm in the directions $\vec{k}_3$ and $\vec{k}_4$. The emission is resonantly enhanced by the diamond level structure that exists in Rb atoms shown in Fig. 1.1b. We collect the pairs into single mode optical fibers and then send them to single photon detectors for analysis.

Pair production from atomic ensembles has received a great deal of attention in recent years. This is due in part to the invention of the quantum repeater [13]

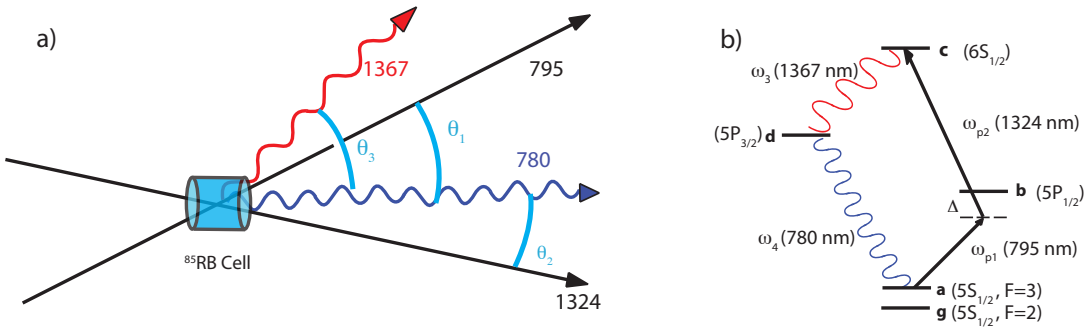

Figure 1.1: a) Schematic of the setup used in the experiment. b) The simplified rubidium diamond level structure.

and more directly the atomic ensemble based quantum repeater (coined the DLCZ scheme for the authors of Ref [26]). Early work came from the groups of Kimble [37, 53] and Lukin [60]. These experiments utilized the lambda level structure in alkali atoms to create nearly degenerate biphotons in the near IR. Work at Stanford in the Harris group has made improvements to the lambda structure generation scheme in cold atoms and has demonstrated new phenomena [25]. Particularly relevant to our discussion is the work of reference [17]. Here the authors use a cascade level structure in a cold atom sample.

It is important to point out the differences of our scheme and that of the references mentioned above. The diamond level structure allows for the generation of pairs that are quite different in frequency from the pump beams. This allows us to use very high quality interference filters to remove pump contamination from the pair modes. The diamond level structure in alkali atoms also allows for pair generation where one photon is at a telecommunications wavelength while the second

wavelength is at a wavelength compatible with an atomic quantum memory and efficient and low noise single photon detectors in the 800 nm region. In the next section we describe an application that takes advantage of this feature. A second possible advantage of our work is that the generation medium we use is technically very simple compared to a cold atom system. This simplification, of course, comes with some disadvantages as well which we will discuss.

1.2 Photon Pairs for Quantum information: Motivation

Quantum mechanically correlated photon pairs, as well as single photon pulses have numerous uses in the field of quantum information science. These include quantum encryption/communicaiton [31] and linear optical quantum computation [35]. The motivation for the work presented here in this thesis is based on the ideas of quantum communication and particularly the quantum repeater [26].

Long distance quantum communication, which is intrinsically secure, relies on the distribution of entanglement over large distances. The best known technology to share entanglement is pairs of entangled photons. Unfortunately, terrestrial communication relies on light transmission through optical fibers, which attenuate the signals in distances of just a few tens of kilometers. Alternatively, quantum key distribution may be performed over free space but this requires the two communication stations to be in line of sight and is plagued by other environmental disruptions. Thus fiber based communication has received the majority of the attention. For classical communication fiber loss is overcome by measuring, amplifying, and resending

the signal. A similar technique cannot work for single sets of entangled photon pairs due to the No-Cloning theorem of quantum mechanics [62]. The quantum repeater solves this problem.

The goal of the repeater is to establish entanglement between two distant quantum memories (ensembles of atoms in the DLCZ protocol). The scheme works by inserting relay stations, each one containing two atomic memories, roughly uniformly between the two target ensembles. Optical fibers link each of the relay stations. The attenuation in optical fibers is minimum at 1550 nm with a value 0.2 dB/km. This can be translated to an exponential attenuation length of $L_{att} = 22$ km. Optimal relay station separation is generally a few times L_{att}. Figure 1.3 shows a schematic of the DLCZ protocol. Black dots represent atomic ensembles. The initial entanglement is denoted by the lines connecting the ensembles. The next step is entanglement swapping which is represented by the ovals. Once the swap has taken place the entanglement is transfered to pairs that are twice as far apart. Subsequent swapping operations are performed until two target atomic memories, which can in principle be very far from one another, are entangled. Experimental realizations of the protocol have been performed over a distance of several meters [19, 63].

The attenuation in the fibers depends on the wavelength of the light. Figure 1.3 shows the attenuation curve as a function of wavelength. Minimum absorption occurs at 1550 nm. The dispersion in the optical fiber can also have an adverse effect on communication by limiting the rate at which pulses may be sent and still be discernible. Minimum dispersion occurs around 1310 nm. Clearly it would

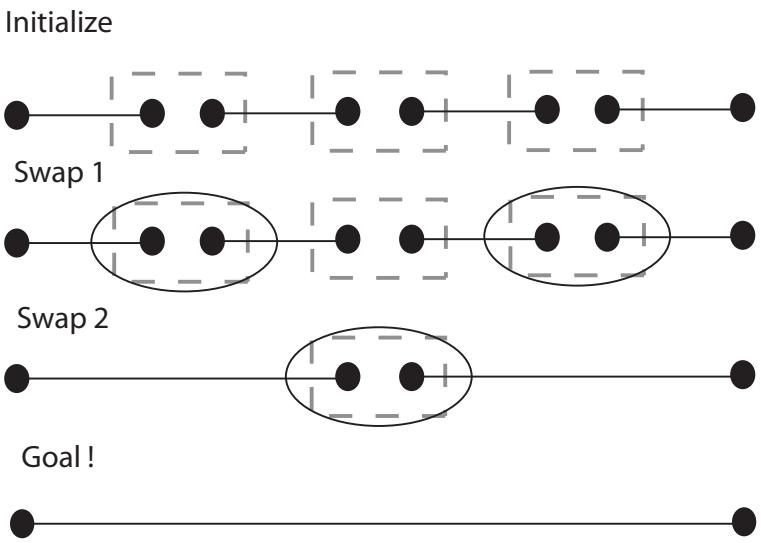

Figure 1.2: The entangling scheme for the DLCZ protocol. The dots denote quantum memories. Pairs connected by lines are entangled. By successive entanglement swapping operations entanglement can be created by pairs very far apart.

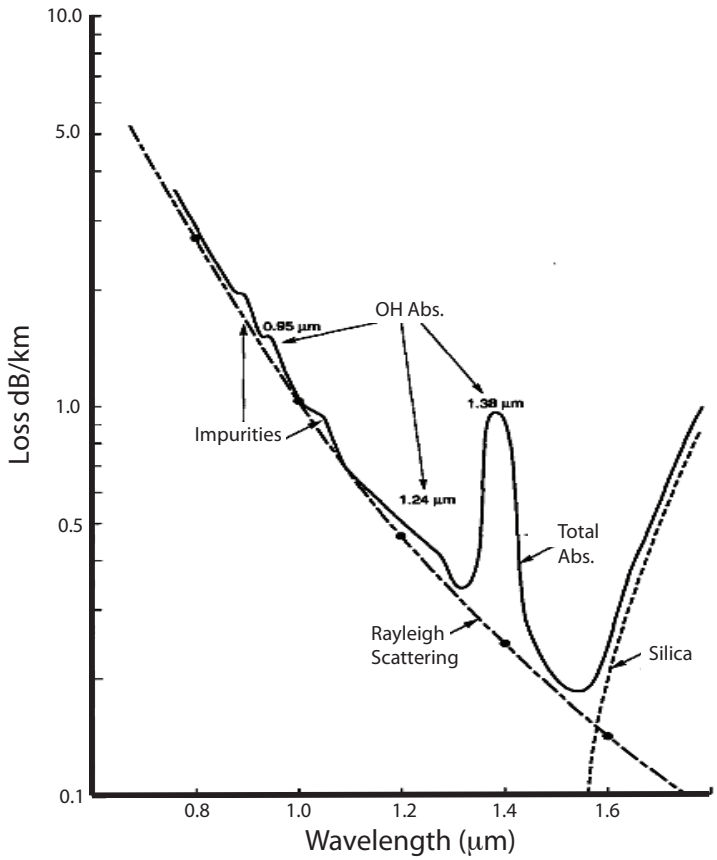

Figure 1.3: Power attenuation in optical fiber. Two telecom windows exist at 1310 nm and 1550 nm.

be beneficial if the light in the fiber was near one of the two telecommunications wavelength windows; however, the other photon involved must be compatible with the atomic quantum memories. The source we discuss here, in principle, meets these requirements. The next section explains in some detail the steps to implement a telecom quantum repeater with alkali atomic memories. The task is technically difficult and requires efficient quantum memories at the single photon level with long storage times which have yet to be demonstrated at the level required for the application, however recent experimental work has shown promising progress[64, 56].

Telecom Quantum Repeater

Figure 1.4 shows in principle how to build a two link quantum repeater with a pair source like the one considered in this work. The first step in the protocol is to establish pairwise entanglement between adjacent locations, separated by some distance on the order of the fiber attenuation length. For this example, this means putting ensemble SE-LI and SE-L in an entangled state, and putting SE-RI and SE-R in an entangled state. Considering just the set on the left, the initial step is to create the entangled state $|\psi_L\rangle = \frac{1}{\sqrt{2}}(|0_{\mathrm{L}}1_{\mathrm{LI}}\rangle + |1_{\mathrm{L}}0_{\mathrm{LI}}\rangle)$, where 0 represents no excitation in the storage ensemble and 1 represents a single collective excitation in the particular storage ensemble. This state is achieved by applying a 4WM pumping pulses to the generation ensemble at both locations synchronously. The pump is weak enough that the probability of generating one pair at 780 nm and 1367 nm is very low. The 1367 nm photons are directed into a single mode fiber and are sent some distance on to a 50/50 beamsplitter and then on to a pair of detectors, D1L and D2L. The 780 nm photons each head to atomic memories, SE-L and SE-LI, where they are stored as a polariton using slow and stopped light techniques [16, 40]. If either detector D1 or D2 registers a count we know that a 780 nm photon is stored in either SE-L or SE-LI and the desired state is achieved. At the same time an identical process has been going on in the right set of storage ensembles and thus upon a click on D1R or D2R we project into the state $|\psi_R\rangle = \frac{1}{\sqrt{2}}(|0_{\mathrm{R}}1_{\mathrm{RI}}\rangle + |1_{\mathrm{R}}0_{\mathrm{RI}}\rangle)$. The entire system is described at this point by $|\psi\rangle = |\psi_L\rangle\,|\psi_R\rangle$.

The next step is the entanglement swapping operation which is denoted in

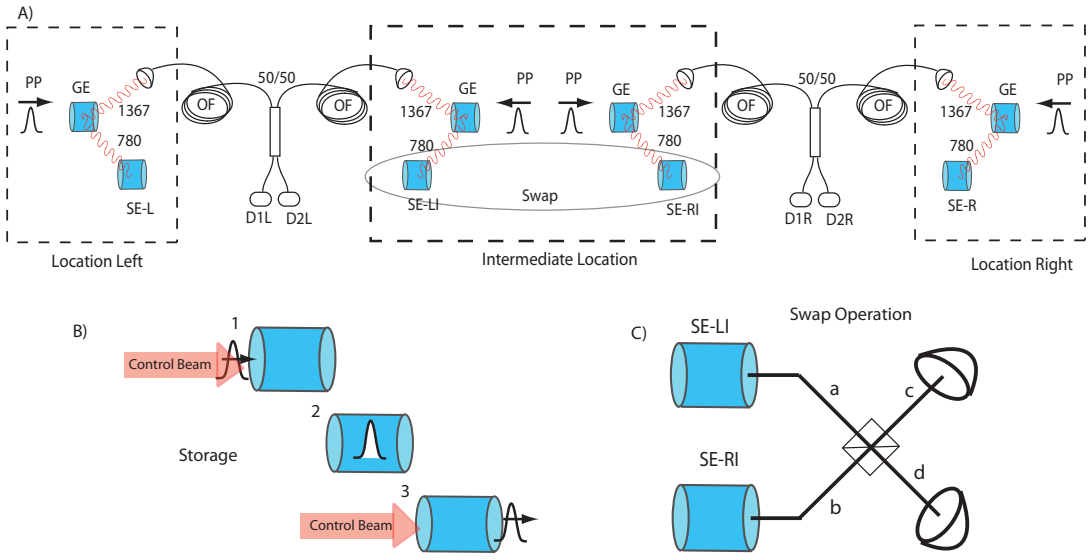

Figure 1.4: a) The DLCZ scheme operating at telecom wavelengths. b) Polariton storage: When the control beam is turned off the group velocity of the pulse in the medium goes to zero. Turning the control beam back on releases the stored pulse. c) The beamsplitter arrangement for the swap operation.

Fig. 1.4 by the oval around SE-LI and SE-RI. This step involves reading out each memory by converting the stored single photon 780 nm pulse back into light and then combining them onto a beamsplitter. I will write out the steps here since I have never seen it done in the literature. The state transforms according to

$$\begin{aligned} |\psi_L\rangle |\psi_R\rangle &\xrightarrow{\text{READ}} \tfrac{1}{2}\left[|0\rangle |1_L 1_R\rangle + \hat{b}^\dagger |0\rangle |1_L 1 0_R\rangle + \hat{a}^\dagger |0\rangle |0_L 1_R\rangle + \hat{a}^\dagger \hat{b}^\dagger |0\rangle |0_L 0_R\rangle\right] \\ &\xrightarrow{\text{BS}} \tfrac{1}{2}\Big[|0\rangle |1_L 1_R\rangle + \hat{c}^\dagger |0\rangle \tfrac{1}{\sqrt{2}}\left(|1_L 0_R\rangle + |0_L 1_R\rangle\right) + \dots \\ &\qquad \hat{d}^\dagger |0\rangle \tfrac{1}{\sqrt{2}}\left(|1_L 0_R\rangle - |0_L 1_R\rangle\right) + \tfrac{1}{2}\left(\hat{c}^{\dagger 2} - \hat{d}^{\dagger 2}\right)|0\rangle |0_L 0_R\rangle\Big] \ . \end{aligned} \tag{1.1}$$

Here, READ means the action of converting the excitations in SE-LI and SE-RI back into light. The action BS corresponds to the retrieved light pulses from each storage ensemble interfering on a 50/50 beamsplitter. Figure 1.4c shows the convention for the fields going into and out of the beamsplitter.

The final expression shows that if a photon is measured in the c-mode or d-mode the resulting state is the maximally entangled state that we are after, $\frac{1}{\sqrt{2}}\left(|1_L 0_R\rangle \pm |0_L 1_R\rangle\right)$. This outcome occurs with probability $\frac{1}{2}$. This leave a $\frac{1}{2}$ probability for failure which can happen in two ways. No detection events we occur $\frac{1}{4}$ of the time. Alternatively, two photons may impinge on a single detector, but due to Hong-Ou-Mandel interference [58, 52] both photons go the same way. A single photon counting detector such as an avalanche photodiode, which cannot tell the difference between 1 and 2 photons, will give a false positive $\frac{1}{4}$ of the time. In this case subsequent operations would eventually give a null detection and the process would be started again. A large amount of work is currently going into detectors with photon number resolution [55] which have the ability to add

This example is for a DLCZ with only 2 links. This can be extended to larger distances. Consider a telecom quantum repeater with N links of length L. We will assume we are using number resolving detectors so that each excitation pulse can be optimally strong and to make things a little simpler. Then we let p be the probability of creating a pair of photons at either site per pump pulse and R be the rate of excitation pulses. Let δ_D be the efficiency of our detector and δ_m be the efficiency of the quantum memory. Then the time it would take to create entanglement between two distant ensembles, separated by $L_o = NL$, is given by

$$T_{tele} = \frac{1}{R\delta_m\delta_D p e^{-\frac{L_o}{NL_{att}}}} \frac{1}{\left(\frac{\delta_D}{2}\right)^{N-1}} \ . \tag{1.2}$$

The same equation is true for a traditional quantum repeater but with $\delta_m = 1$ since storage is built into the initialization step. Now we may compare a telecom quantum repeater operating at 1324 nm to one at currently storable wavelengths operating at 780 nm. The 780 nm repeater will be far worse but it is interesting to see just how much worse. To make the comparison we have to pick the optimal number of relay stations at each total distance. Figure 1.5 shows the entangling time as a function of total distance with all things equal except the $L_{att} = 1.45$ km for the telecom photons while at 780 nm $L_{att} = 14.5$ km. The optimal number of links is written above some of the points. For comparison the result for direct communication is plotted on the same graph. For this example $\delta_m = 0.01$ which shows that even for a relatively inefficient memory the extra storage step for the telecom repeater is inconsequential.

A quantum repeater based on telecommunications wavelength photons far out-

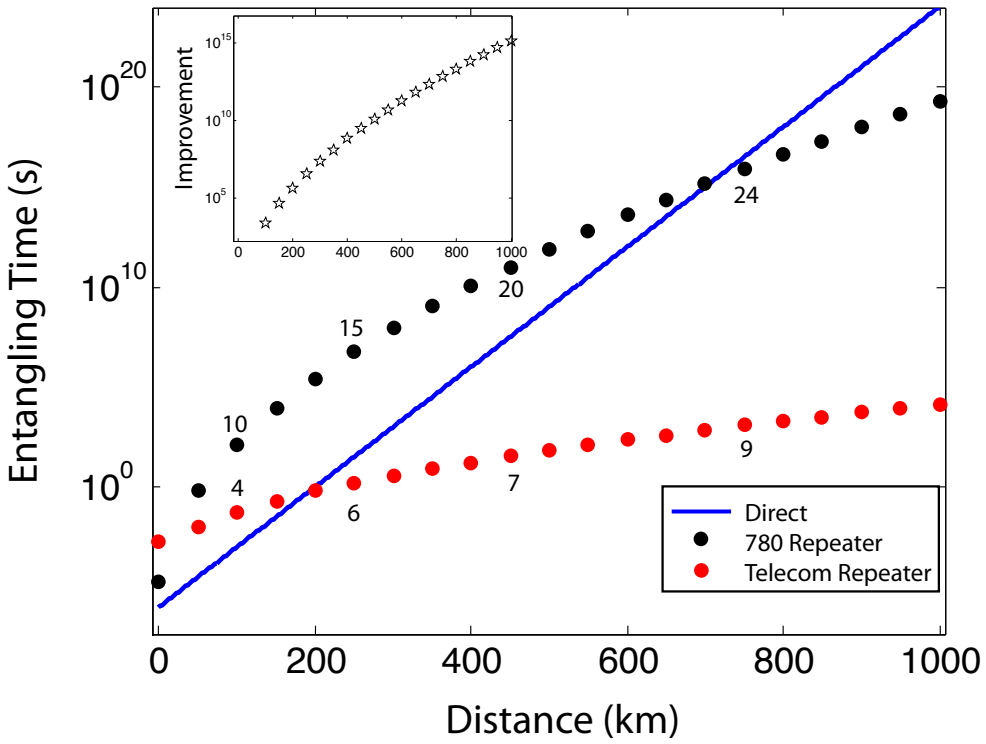

Figure 1.5: a) The entangling time as a function of distance for a quantum repeater operating at telecom and at 780 nm. Also plotted is the result for a direct distribution scheme. The inset shows the improvement factor for the telecom repeater. The numbers above the points indicate the number of links that are required to minimize the entangling time. The numbers used here are $R = 10^6$ Hz, $\delta_D = 0.6$, and $p = 0.3$

performs one that works with currently storable photons. We should note that all demonstrations of DLCZ schemes to this point have been done at 780 nm or 852 nm. The quantum repeater diagramed in Fig. 1.4 is currently beyond the state of art for experimental physics. For the example above the entangling time is 1 s at 250 km and 1233 s at 750 km. This time has to be compared to the decoherence time of the quantum memories, which for now is limited to several ms for atomic gases. It should also be compared to how long you are willing to wait for an encryption key. For a telecom quantum repeater working at 1550 nm and with 95% detection efficiency and 95% memory efficiency the entangling time at 750 km is 37 ms. Thus improvements in detectors and quantum memories can push DLCZ schemes closer to reality. The work of this thesis investigates a source of photon pairs that could in principle be used in such an application.

1.3 Outline

This work aims to understand the properties of the photon pairs created by spontaneous 4WM in a warm atomic ensemble of Rb using the diamond level configuration of Fig. 1.1. Chapter 2 presents measurements and theory concerning semi-classical 4WM from Rb-vapor. This preliminary work gives an understanding of the basic resonance structure of the 4WM interaction, the efficiency of the process, and the effects of the thermal motion of the atoms on the non-linear and linear response of the system. Chapter 3 considers pair generation from the medium. We discuss the experimental setup and present the cross correlation function for dif-

ferent pump laser parameters. The temporal profile of the correlation function is clearly modified by the pump laser conditions and we present a model that shows qualitative agreement with some of our measurements. Chapter 4 shows violation of Bell's inequality as well as the Cauchy-Schwarz inequality, definitively demonstrating polarization entanglement and non-classical correlation of the pairs. We examine the system as a source of heralded single photons. Chapter 5 ends with some general remarks and conclusions.

Chapter 2

Semi-Classical Four-Wave Mixing in the Diamond Configuration

2.1 Introduction

In this chapter we are concerned with the the properties of the semiclassical 4WM interaction in an atomic vapor of Rubidium. In the following experiments we apply three lasers to the atomic ensemble and as a function of the pump laser parameters observe the variation of the intensity of the light generated at 1367 nm. We do these measurements to understand the resonance structure of the 4WM in the Doppler broadened media in this particular level configuration. We measure the efficiency of the 4WM process and see that it is limited by linear absorption.

Four-wave mixing (4WM) in atomic vapors has been explored extensively in the past. Some of the original work investigated basic nonlinear optics, interference phenomena among various optical processes [10], and the generation of squeezed light [59]. Recent work in 4WM in atomic vapors has lead to large twin-beam multi-mode squeezing with applications to quantum imaging [12, 11].

Much of the recent literature has exploited the Λ or double-Λ atomic level structure which benefits from long lived coherence between the two lower stable states. Here we concern ourselves with a warm ensemble of atoms in the diamond configuration, illustrated in Fig. 2.1a. The diamond level structure has one stable ground state, two intermediate levels, and one top state, pairwise coupled by the

electromagnetic field as indicated. Earlier theoretical work has shown that this level structure gives rise to interesting phase sensitive propagation behavior [49]. The work that we present here appears in two papers. The first paper examines the complicated resonance structure of a strongly driven diamond system [5]. The second paper examines the resonant structure due to Doppler effects and the efficiency of the 4WM process [61].

The 4WM interaction can be considered as an interference effect. In our case three laser beams interact with a collection of atoms which serve to excite a dipole moment in the atoms with a spatially varying phase. The atoms then radiate and if the spatially varying phase is correct, the dipole radiation from each atom interferes constructively in a specific direction. In our case fields 1 (795 nm), 2 (1324 nm), and 4 (780 nm) are incident on the atoms with frequencies ω_1, ω_2, and ω_4 and wave-vectors $\vec{k}_1$, $\vec{k}_2$, and $\vec{k}_4$. The generated field 3 (1367 nm) has frequency ω_3 and wave-vector $\vec{k}_3$. Conservation of energy requires that

$$\omega_1 + \omega_2 = \omega_3 + \omega_4 \ . \tag{2.1}$$

For our configuration the dipole moment responsible for the generated light is proportional to $\exp\left(i\vec{r}\cdot\left(\vec{k}_1 + \vec{k}_2 - \vec{k}_4\right)\right)$ which results in constructive interference in the $\vec{k}_3$ direction such that

$$\vec{k}_1 + \vec{k}_2 = \vec{k}_3 + \vec{k}_4 \ . \tag{2.2}$$

Equation 2.2 is called the phase-matching condition and must be satisfied for optimum 4WM gain.

In addition to the conservation of linear momentum and energy an additional

conservation law, conservation of angular momentum, must apply to the system. This gives rise to polarization correlations which, as we will see in chapter 4, lead to polarization entangled pair emission under the conditions of spontaneous 4WM.

2.2 The Experimental Setup

For the work presented in this chapter there are 3 lasers involved, an isotopically pure rubidium 85 cell, and Si (for 780 and 795 nm) and InGaAs (for 1324 and 1367 nm) amplified photo diodes. Below we briefly discuss some of the experimental details including the geometry.

The Lasers

The 795 nm laser is a Coherent 899-01 titanium-saphire (Ti-Saph) ring laser pumped by a green Coherent Verdi. The pump laser puts out a maximum of 10 W of power at 532 nm which ends up producing > 500 mW of 795 nm light which is more than enough for the experiment. The Ti-Sapph laser has thin and a thick etalons to narrow the linewidth. They are manually tuned and kept at a given temperature with a feedback control system. The home built feedback system, explained later, only acts on a piezo electric mounted mirror (the tweeter mirror). We lock the laser to a saturated absorption line in the D1 transition of Rb. We adapt the Pound Dreever Hall technique [23, 8] to this resonance to obtain an error signal. The probe beam of the lock setup passes through a phase modulator that provides sidebands at 15 MHz, then through the atoms, and finally onto a silicon photodiode. We amplify

and mix down the signal from the photodiode to extract the error signal. The feedback is supplied by an off the shelf P-I lockbox (Precision Photonics LB1005, now sold by New Focus), which drives a high voltage amplifier which controls the tweeter mirror piezo voltage.

The 795 nm laser is fiber coupled near the output of the laser into a polarization maintaining single mode fiber and then back out into free space. This eliminates the need to realign the experiment every time the laser needs adjusting. We intensity stabilize the light after the fiber using an acousto-optic modulator (AOM) and on some occasions a slow mechanical polarization rotator with a computer handling the feedback. We have measured the line-width of the laser to be less than 500 kHz using a self-heterodyne set up [51].

The 1324 nm laser is an external cavity grating stabilized diode laser from EOSI (the company has been absorbed by Newport Optics). The laser is frequency locked using a digital transfer lock [65]. The scheme uses a Melles-Griot frequency stabilized Helium Neon laser as a stable frequency reference. We put the HeNe through a confocal Fabry-Perot (FP) cavity with mirrors separated by 25 cm and with moderate (≈ 100) finesse at two wavelengths: 632 nm and 1324 nm. We scan the cavity and digitize the transmission of the HeNe beam. A small amount of 1324 nm light also goes through the cavity and the transmission is also digitized. By comparing the FP peaks from each laser and relying on the HeNe stability we can derive an error signal with the computer and feedback to the 1324 nm laser. We also servo the average length of the cavity to counteract temperature drift in the room. The lock is quite slow with bandwidth of roughly 5 Hz but it has been sufficient for

our needs. The lock could be sped up by changing a few settings on the software. We are able to achieve stability on the order of a few MHz for hours. The linewidth of the laser was measured to be ≈1 MHz.

The third laser is a 780 nm diode. The diode resides in a Thorlabs TCLDM9 diode head. We control the temperature of the diode using the internal thermoelectric cooler of the diode head and a Tholabs TED200 temperature controller. The current is supplied by a home built current driver based on a 1997 JILA design. The diode is a Sharp GH0781JA2C which free-running puts out around 100 mW and has a line width of less than 10 MHz [44]. This laser can be locked by a dichroic atomic vapor laser lock (DAVLL) [21] or by saturation spectroscopy in the same manner as the Ti-Saph, but for the work that we will present here we do not lock this laser and instead scan it over the resonances.

The Atoms

The level structure we use in all our work is the diamond structure shown schematically in Fig. 2.1a. The detailed structure of ^{85}Rb is shown in Fig. 2.1 which includes all the hyperfine structure as well as the Zeeman sublevels. The rubidium cell is a 1.5 cm evacuated glass cell containing isotopically pure ^{85}Rb metal. The vapor pressure above the metal serves as our interaction medium. By controlling the temperature of the cell with a resistive heater we can change the vapor density between 7×10^9 cm^{-3} at room temperature to 1×10^{13} cm^{-3} at 115 °C.

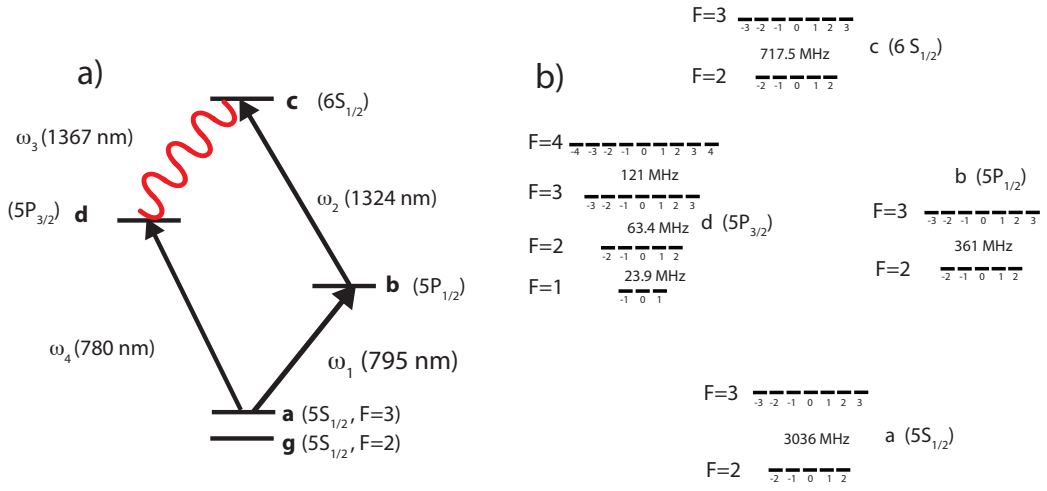

Figure 2.1: a) Rubidium level structure and the applied lasers. b) Detailed Rb structure including all hyperfine and Zeeman sublevels.

The Beam Geometry

Figure 2.2a shows the nearly co-propagating geometry we use. We pick the angles to satisfy the phase-matching condition of Eqs. 2.2 and maximize overlap region in the medium while still being able to separate the beams after the cell. Another reason to select nearly co-propagating or counter-propogating beams is Doppler selectivity.

Consider the case where two beams intersect at 90°, to take the most extreme situation, and require that both be resonant with two separate transitions in a thermal cell of atoms. Then only one velocity class moving into beam 1 can be resonant at once. But only one velocity class moving into or out of beam 2 can be resonant with that transition. This means that the Doppler profile must be cut twice, once in the direction of beam 1 and once in the direction of beam 2. This results in very few atoms that can satisfy both resonance conditions at once. This type of multi-transition resonance must be fulfilled for efficient 4WM so we choose a co-propogating geometry.

Both the 795 nm and 1324 nm beams are horizontally polarized. The polarization of the generated beam is then the same as the 780 nm laser polarization, which we arbitrarily chose to be vertical. The efficiency of the process does not depend strongly on the choice of 780 nm pump polarization. All the beams have approximately gaussian profiles with waists of ≈ 1 mm.

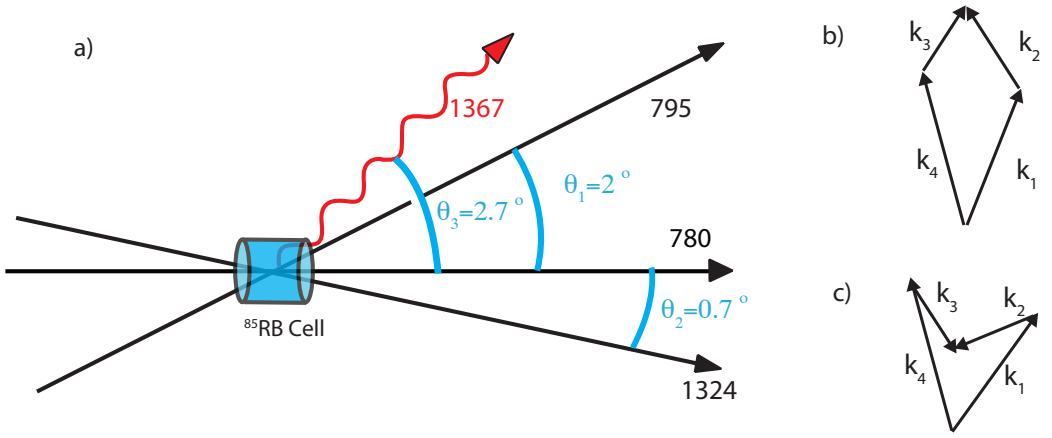

Figure 2.2: a) The geometry we use in the experiment. The angles of the beams are $\theta_1 = 2^o$, $\theta_2 = 0.7^o$, and $\theta_3 = 2.7^o$. b) Phase-matching geometry similar to what we use and c) another example with larger angles between the beams.

2.3 Experiment: 4WM Resonance Structure

The first experiment we will consider aims to measure the resonance structure of the 4WM in two separate pumping regimes. First, we observe the intensity of the generated light at 1367 nm as a function of the detuning of the 1324 nm and 780 nm lasers when the 795 nm laser is locked 1.5 GHz red-detuned from the D1 line. We scan the 1324 nm laser across the two-photon resonance and the 780 nm laser across the D2 Doppler peak. In Fig. 2.3 we plot the intensity of the generated 1367 nm light which exhibits a narrow Gaussian-like resonance.

Figure 2.4 shows a slice of the surface plotted in Fig. 2.3 at a constant 1324 detuning. We lock the 795 nm laser 1.5 GHz red of the D1 line while the 1324 nm laser is locked such that the two lasers together are resonant with the ($5S_{1/2}$, F=3) $\rightarrow$ ($6S_{1/2}$, F=3) two-photon resonance. The 1324 nm laser is locked using the digital

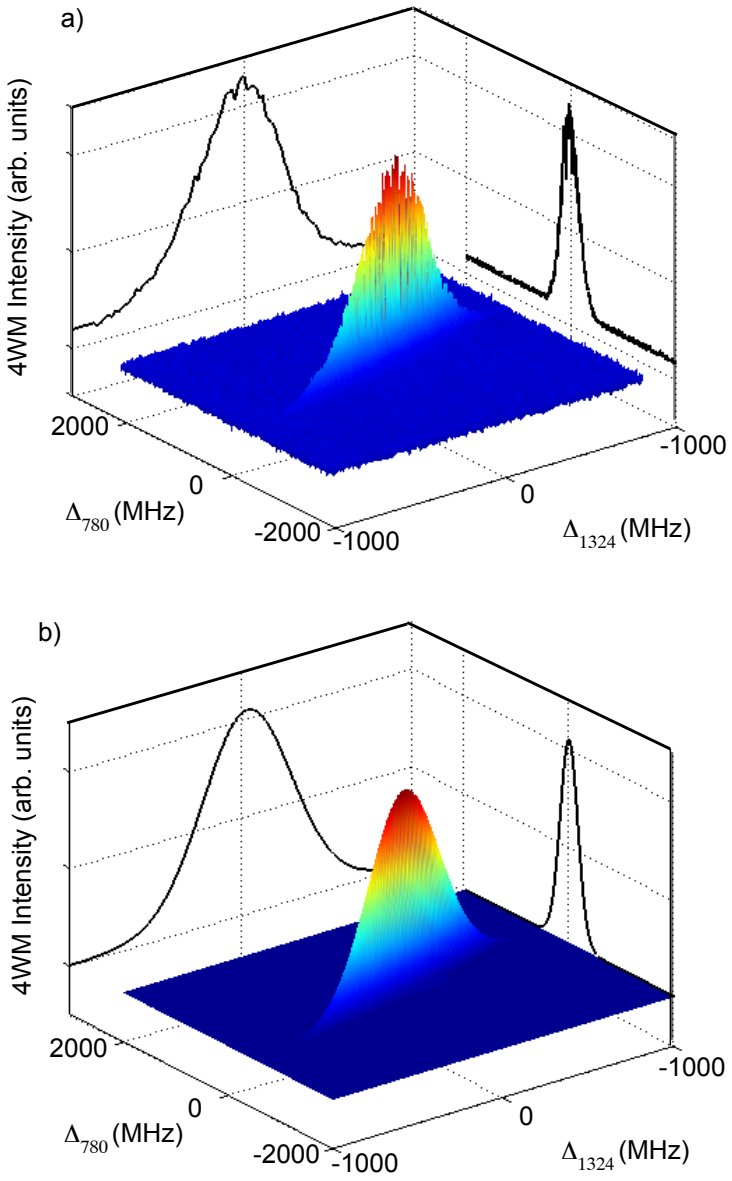

Figure 2.3: Generated 1367 nm intensity as a function of 780 and 1324 detuning. The narrow feature is a result of velocity class selection. For this example $P_{780} = 3\text{mW}$, $P_{795} = 100\text{mW}$ and $P_{1324} = 5\text{mW}$. The 795 nm laser was detuned 1.5 GHz red of the D1 F=3 $\rightarrow$ F=2,3 peak. The data appears in a), b) is our model (discussed below).

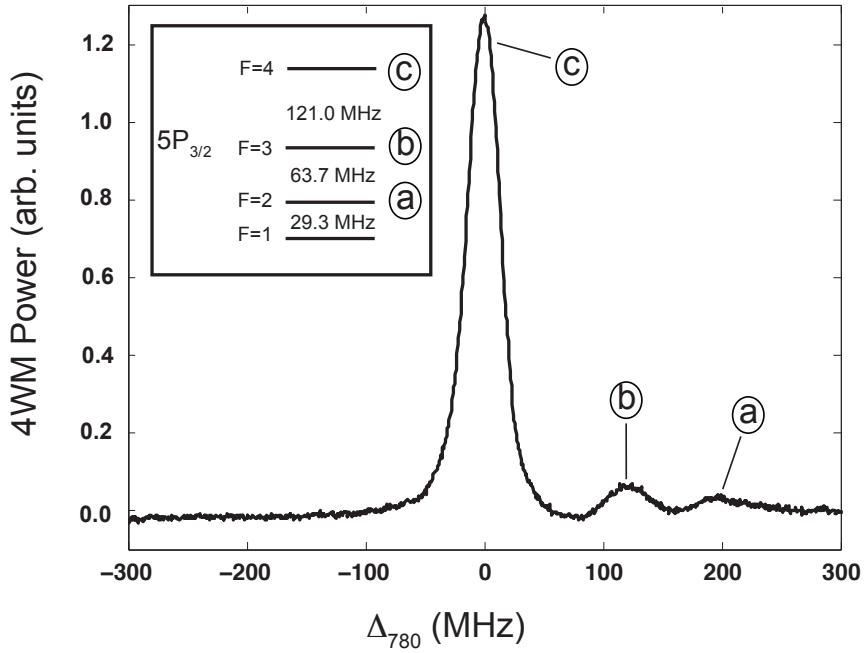

Figure 2.4: The intensity of the generated 1367 nm beam as a function of 780 nm detuning. The inset shows the $5P_{3/2}$ hyperfine structure which is the origin of the 3 observed peaks.

transfer-cavity lock. We scan the 780 nm laser over the D2 line. There are three peaks in the 4WM signal corresponding to the three allowed intermediate hyperfine states. The largest peak involves the F=4 intermediate state. The asymmetry in the peaks already points to optical pumping effects in the system that contribute significantly to the details of the semiclassical and quantum analysis.

In a second measurement we put the 795 nm laser on resonance with the $5S_{1/2}$ F=3 $\rightarrow$ $5P_{1/2}$ F=2 transition. We scan the 780 nm and 1324 nm laser as before and measure the 1367 nm light. The 795 nm pump laser power is well above saturation intensity and thus we would expect to see Autler-Townes style splittings [3] in the

4WM resonance structure (see Fig. 2.5a).

2.4 Experiment: Generation Efficiency

It is important to consider the efficiency of conversion from 780 nm photons to 1367 nm photons for application in various quantum communication protocols. Figure 2.6 shows the power in the generated light as a function of the power in the 780 beam for several different 795 laser powers. The efficiency is never greater than 10^{-4}, due to the absorption of the medium (See Sec. III). The residual magnetic field (< 1 G) does not affect the efficiency in any significant way.

2.5 Theory and Analysis

We are concerned in this section with understanding the origin of the sharp peak in Fig. 2.3a and the efficiency of the 4WM process. To this end we apply the density matrix formalism and solve the Maxwell-Bloch equations [9].

2.5.1 Maxwell-Bloch Treatment

We model the system with the standard density matrix treatment including spontaneous decay. We have a four level atom with the structure indicated in Fig. 2.1a. Our atoms are coupled to an electromagnetic field of the form

$$E(z,t) = \sum_{i=1}^{4} (E_i(z) e^{i(k_i z - \omega t)} + c.c.) \; . \tag{2.3}$$

We use the notation indicated in Fig. 1 in which the generated beam is of frequency $\omega_3 = \omega_1 + \omega_2 - \omega_4$. The propogation direction of each laser is given by $\vec{k}_i$ where

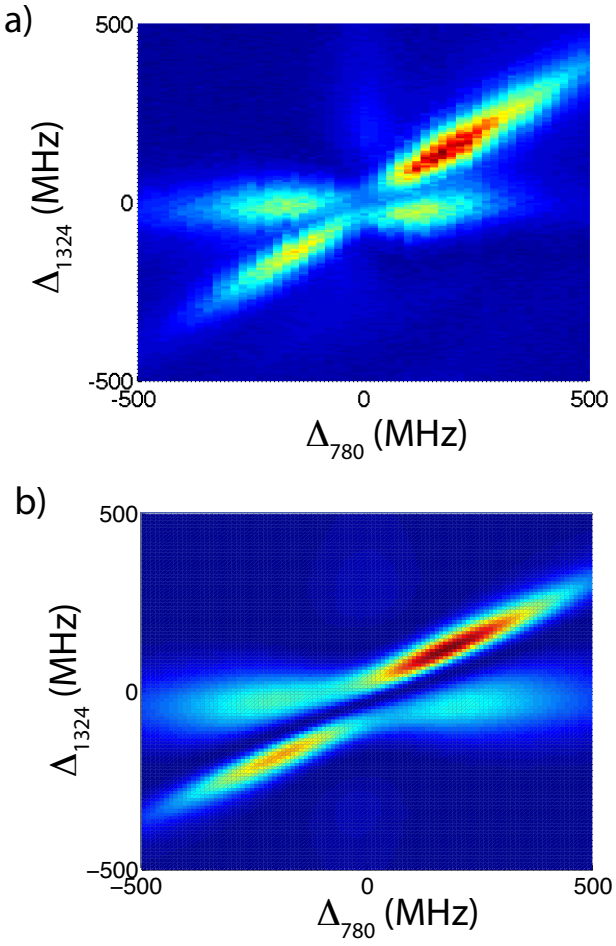

Figure 2.5: Generated 1367 nm intensity as a function of 780 and 1324 detuning with $P_{780} = 3\text{mW}$, $P_{795} = 100\text{mW}$, and $P_{1324} = 5\text{mW}$. The 795 nm laser is nearly resonant with the zero velocity class the D1 F=3 $\rightarrow$ F=2,3 peak. The data appears in a), b) is our model (discussed below).

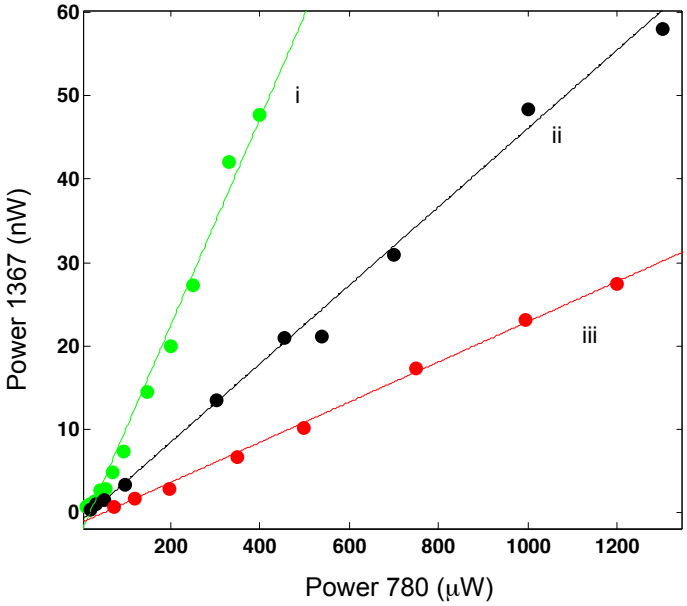

Figure 2.6: The power in the generated 1367 nm beam for different 780 powers. Each line is for a different 795 power: i) $P_{795} = 115$ mW, ii) $P_{795} = 50$ mW, and iii) $P_{795} = 15$ mW. The power in the 1324 nm laser is 5 mW and efficiency is between 10^{-4} to 10^{-5} in all cases.

$\left|\vec{k}_i\right| = 2\pi/\lambda_i$. We define the one-photon detunings as $\Delta_{ba} = \omega_{ba} - \omega_1$, $\Delta_{cb} = \omega_{cb} - \omega_2$, $\Delta_{cd} = \omega_{cd} - \omega_3$, and $\Delta_{ba} = \omega_{ba} - \omega_4$. The two-photon detunings are $\Delta_{ca} = \Delta_{cb} + \Delta_{ba}$ and $\Delta_{bd} = \Delta_{ba} - \Delta_{da}$. We define γ_{ij} to be the atomic decay rate in radians per second from level i to j and Γ_{ij} to be the average of the total decay rates from levels i and j. Finally, we define the spatially varying Rabi frequencies $\Lambda_{ba} = E_1(z)e^{i\vec{k}_1 z}\mu_{ba}/\hbar$, $\Lambda_{cb} = E_2(z)e^{i\vec{k}_2 z}\mu_{cb}/\hbar$, $\Lambda_{cd} = E_3(z)e^{i\vec{k}_3 z}\mu_{cd}/\hbar$, and $\Lambda_{da} = E_4(z)e^{i\vec{k}_4 z}\mu_{da}/\hbar$. We also factor out the fast time dependence of the laser fields from the denstity matrix elements such that $\rho_{ij} = \sigma_{ij}\exp(-i\omega_{ij}t)$. With these definitions the density matrix equations become

$$\dot{\sigma}_{aa} = \gamma_{ba}\sigma_{bb} + \gamma_{da}\sigma_{dd} + i(\Lambda_{ab}\sigma_{ba} - \Lambda_{ba}\sigma_{ab}) + i(\Lambda_{ad}\sigma_{da} - \Lambda_{da}\sigma_{ad}) \quad (2.4)$$

$$\dot{\sigma}_{bb} = -\gamma_{ba}\sigma_{bb} + \gamma_{cb}\sigma_{cc} + i(\Lambda_{bc}\sigma_{cb} - \Lambda_{cb}\sigma_{bc}) + i(\Lambda_{ba}\sigma_{ab} - \Lambda_{ab}\sigma_{ba}) \quad (2.5)$$

$$\dot{\sigma}_{cc} = -(\gamma_{cb} + \gamma_{cd})\sigma_{cc} + i(\Lambda_{cb}\sigma_{bc} - \Lambda_{bc}\sigma_{cb}) + i(\Lambda_{cd}\sigma_{dc} - \Lambda_{dc}\sigma_{cd}) \quad (2.6)$$

$$\dot{\sigma}_{dd} = -\gamma_{da}\sigma_{dd} + \gamma_{cd}\sigma_{cc} + i(\Lambda_{dc}\sigma_{cd} - \Lambda_{cd}\sigma_{dc}) + i(\Lambda_{da}\sigma_{ad} - \Lambda_{ad}\sigma_{da}) \quad (2.7)$$

$$\dot{\sigma}_{ab} = -(i\Delta_{ab} + \Gamma_{ab}) + i(\Lambda_{ab}\sigma_{bb} + \Lambda_{ad}\sigma_{db}) - i(\Lambda_{ab}\sigma_{aa} + \Lambda_{cb}\sigma_{ac}) \quad (2.8)$$

$$\dot{\sigma}_{ac} = -(i\Delta_{ac} + \Gamma_{ac}) + i(\Lambda_{cb}\sigma_{bc} + \Lambda_{ad}\sigma_{dc}) - i(\Lambda_{bc}\sigma_{ab} + \Lambda_{dc}\sigma_{ad}) \quad (2.9)$$

$$\dot{\sigma}_{ad} = -(\gamma_{cb} + \gamma_{cd})\sigma_{cc} + i(\Lambda_{cb}\sigma_{bc} - \Lambda_{bc}\sigma_{cb}) + i(\Lambda_{cd}\sigma_{dc} - \Lambda_{dc}\sigma_{cd}) \quad (2.10)$$

$$\dot{\sigma}_{bc} = -\gamma_{da}\sigma_{dd} + \gamma_{cd}\sigma_{cc} + i(\Lambda_{dc}\sigma_{cd} - \Lambda_{cd}\sigma_{dc}) + i(\Lambda_{da}\sigma_{ad} - \Lambda_{ad}\sigma_{da}) \quad (2.11)$$

$$\dot{\sigma}_{bd} = \gamma_{ba}\sigma_{bb} + \gamma_{da}\sigma_{dd} + i(\Lambda_{ab}\sigma_{ba} - \Lambda_{ba}\sigma_{ab}) + i(\Lambda_{ad}\sigma_{da} - \Lambda_{da}\sigma_{ad}) \quad (2.12)$$

$$\dot{\sigma}_{cd} = -\gamma_{ba}\sigma_{bb} + \gamma_{cb}\sigma_{cc} + i(\Lambda_{bc}\sigma_{cb} - \Lambda_{cb}\sigma_{bc}) + i(\Lambda_{ba}\sigma_{ab} - \Lambda_{ab}\sigma_{ba})\,. \quad (2.13)$$

We can write these equations in the form $R\vec{\sigma} = \dot{\vec{\sigma}}$ where R is a 16×16 matrix and $\vec{\sigma}$ is a length-16 vector containing the elements of the density matrix. In the steady

state this reduces to $R\vec{\sigma}_s = 0$. Because of conservation of population the rows R are not independent and therefore we replace the σ_{aa} equation with the trace condtion, $\Sigma_i \rho_{ii} = 1$. Then the equation to solve is $R\vec{\sigma}_s = \vec{y}$, where $\vec{y} = (1\ 0\ 0\ 0\ ...)^T$.

Note that since we are discussing a thermal ensemble of atoms, the motion of the atoms will be an important factor in the emission spectrum. Atomic motion can be included through the Doppler shift of the various laser detunings for each velocity v, *e.g.* $\Delta_{ba}^v = \omega_{ba} - \omega_1 + \vec{k}_1 \cdot \vec{v}$. Integrating each density matrix element over the one dimensional Boltzman distribution then gives

$$\bar{\sigma}_{ij} = \int \rho(v)\sigma_{ij}(v)dv \ , \tag{2.14}$$

where $\rho(v) = \sqrt{m/(2\pi k_b T)}\exp(-mv^2/(2k_b T))$.

In some cases it is sufficient to calculate the steady state polarization of the medium. In others, particularly when several competing processes are at work, such as 4WM and absorption, one must take propagation into account. For an electromagnetic field propagating in an atomic medium with a polarization of the form

$$P(z,t) = \sum_{i=1}^{4}(P_i(z)e^{-i\omega_i t} + c.c.) \ , \tag{2.15}$$

the wave equation in the slowly varying amplitude approximation becomes

$$\partial_z E_i = 2\pi|k|ie^{-ik_i z}P_i(z) \ . \tag{2.16}$$

The atomic polarization is related to the density matrix through $P = N\langle\mu\rangle = N\mathrm{Tr}(\rho\mu)$. The polarization of the medium that contributes as a source for the 4WM process is $P_3(z) = N\mu_{dc}\bar{\sigma}_{cd}$, with similar expressions for the other P_i. We

solve the coupled set of equations for the field and atoms down the length of the atomic ensemble. We neglect any possible transverse effects.

Figure 2.7 shows a typical solution to the MB equations with $\Delta_{ba} = -\Delta_{cb} =$ 1500 MHz$\times 2\pi$. The incident intensities are $I_1 = I_2 = 10$ mW/cm^2 and $I_4 =$ 1 mW/cm^2. Fig. 2.7(a) shows the intensity of fields 3 and 4 as a function of propagation distance in the medium. Linear absorption dominates the behavior of field 4 while parametric 4WM leads to the generation of field 3. In Fig. 2.7 (b) we see the polarization of the generated beam, P_3, as a function of propagation distance and velocity of the the atoms in the medium. The polarization decreases as a function of length due to the absorption of the field 4 while only a narrow band of velocities, centered around $v = 0$ for the parameters used here, contributes to the 4WM process.

2.5.2 Velocity Selective 4WM

Figure 2.3 (b) shows a plot of $|\sigma_{cd}|^2$ solved numerically for parameters close to that of the experiment. For large detuning of the 795 nm field the data and model show a narrow sub-Doppler feature, in clear qualitative agreement.

Intuitively this feature can be explained by the fact that the 4WM process is strongest in resonant atoms. Since we are working in a thermal cell, given a set of proper detunings, only one velocity class (a group of atoms all moving with roughly the same velocity with spread $\sigma_v \approx \gamma/k$, where k and γ are some characteristic wave-vector and atomic line-width, respectively) will be resonant for 4WM at a time. To

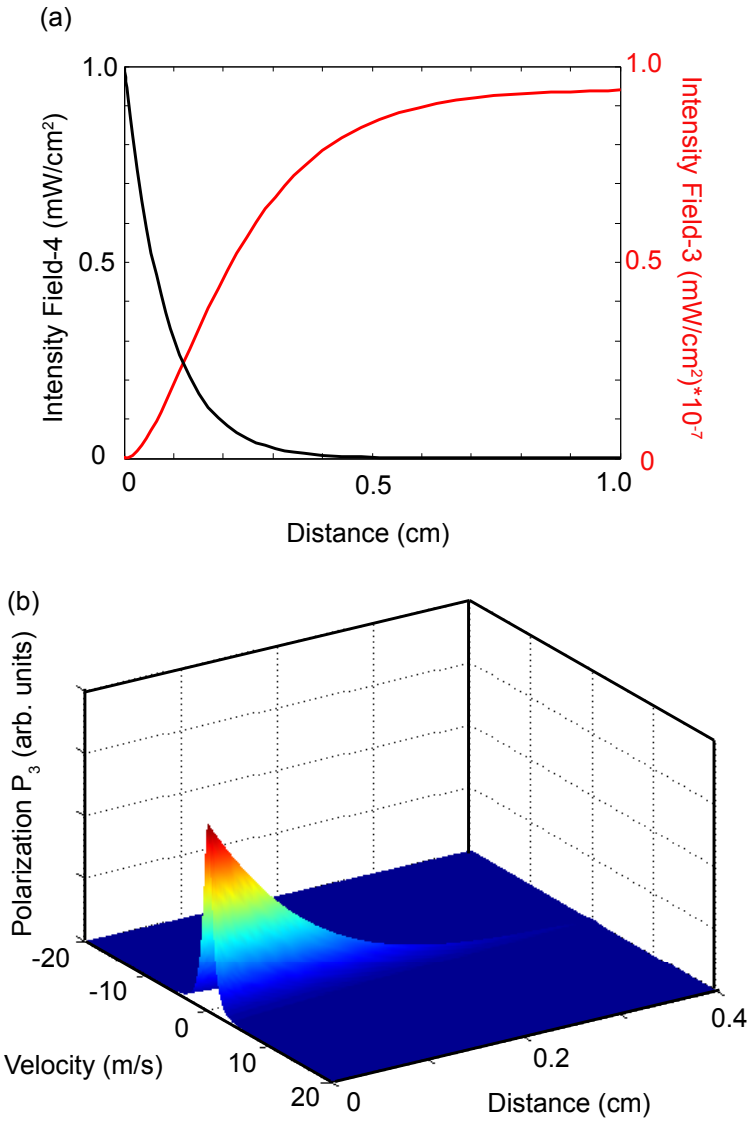

Figure 2.7: Typical solution to the MB equations in the diamond system. (a) The intensity of fields 3 and 4 as a function of propagation distance. (b) The polarization, P_3, of the generated field as a function of propagation distance and velocity class.

lowest nonzero order the solution to Eq. 2.4 for the polarization component which contributes to simple 4WM is proportional to

$$\sigma_{cd}^{PM} = \frac{\Lambda_{ad}\Lambda_{ba}\Lambda_{cd}}{(\Delta_{ba} - i\Gamma_{ba})(\Delta_{da} + i\Gamma_{da})(\Delta_{ca} - i\Gamma_{ca})} , \tag{2.17}$$

where PM stands for phase-matched. In the present case the 795 nm (ω_1) laser is so far off resonance ($\Delta_{ba} \approx 1.5$GHz) that there are essentially no atoms with a velocity large enough to Doppler shift them onto one-photon resonance with that beam. However, some velocity class v_R exists such that the two photon $a \rightarrow c$ transition is resonant. If we then ask what ω_4 must be to be resonant with that same velocity class we are lead to the two equations, $0 = \Delta_{ca} + \vec{k}_{2\gamma} \cdot \vec{v}_R$, and $0 = \Delta_{da} + \vec{k}_4 \cdot \vec{v}_R$. Here $\vec{k}_{2\gamma} = \vec{k}_1 + \vec{k}_2$. We can eliminate v_r and are left with an equation for the 4WM resonance peak position in the $(\Delta_{ca}, \Delta_{da})$ plane,

$$\Delta_{da} = \frac{\left|\vec{k}_4\right|}{\left|\vec{k}_{2\gamma}\right|}\Delta_{ca} . \tag{2.18}$$

For the Rb level structure we use, the slope is $\mathcal{M} = k_4/k_{2\gamma} = 0.637$. We measure the slope of the 4WM feature with two calibrated Fabry-Perot scans for several different detunings of the 795 nm laser, all of which are outside of the single photon Doppler peak. Fig. 2.8 shows a typical measured resonance structure with the best fit line through the maxima. The result is $\mathcal{M}_{measured} = 0.62 \pm 0.02$, which is in agreement with the theory. The slope is calculated from the data by first determining the position of the maxima in the detuning plane then fitting a line to those points. To determine the maxima we fit Lorentzian functions at fixed Δ_{1324} to the data and determine the peak position in the Δ_{780} variable. This fit gives an uncertainty in peak position which leads to the uncertainty in the measured slope.

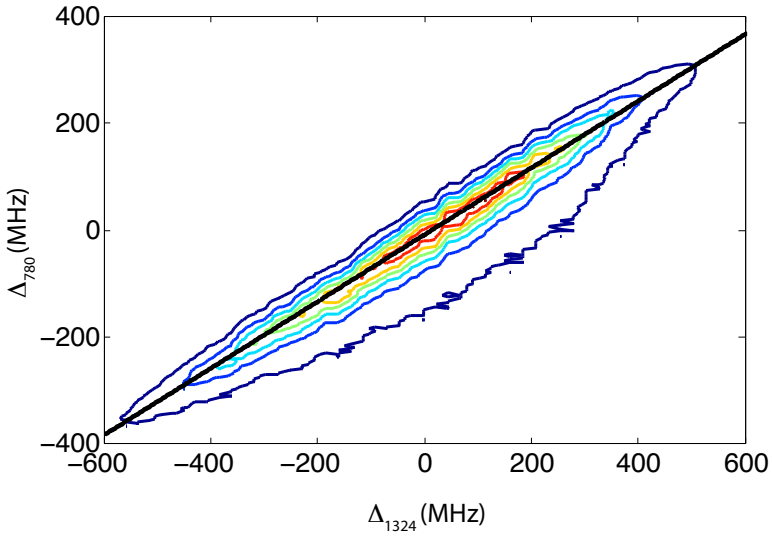

Figure 2.8: A contour plot of the measured intensity of the 4WM as a function of 1324 nm and 780 nm laser frequency. The straight line shows a best fit line through the maxima of the resonance feature. The slope agrees well with the theoretical prediction.

2.5.3 Resonance Structure: Autler-Townes Effects in 4WM

Figure 2.5 shows the experimentally measured and theoretically predicted 1367 nm light intensity as a function of the pump laser detunings. Autler-Townes splitting [3] is a phenomena in which a two-level atom is driven strongly by a resonant pump laser and undergoes an effective level splitting. If either the upper or lower transition is probed by another laser from some other auxiliary level, the line we be split by the Rabi frequency of the pump laser. This effect is closely related to the Mollow triplet observed in the fluorescence spectrum of a driven two-level atom [48]. The same physical effect manifests itself as splittings in the 4WM resonance structure as can be seen in Fig. 2.5. The splitting can be described by a Schrödinger equation treatment which is the subject of a Ref. [5].

2.5.4 Conversion Efficiency

We define the conversion efficiency of the 4WM process as $\mathcal{E} = I_3(L_{cell})/I_4(0)$. This is the ratio of the generated 1367 nm light to the 780 nm pump. The efficiencies measured in the experiment are presented in table 2.1. One could solve the MB equations with parameters similar to that in the experiment, namely a cell of length $L = 1.5$ cm at temperature $T = 90$ °C and pump powers $P_{795} = 15$ mW and $P_{1324} = 5$ mW. However, the answer is highly dependent on the choice of dipole moments. Since the model we are solving is only a 4 level approximation (ignoring the hyperfine and Zeeman sublevel structure) , we cannot expect it to give an accurate estimate of the efficiency.

Table 2.1: Measured experimental 4WM generation efficiencies with $P_{1324} = 5$ mW.

795 nm Power (mW)	Efficiency
115	13×10^{-5}
50	4.5×10^{-5}
15	2.4×10^{-5}

A full Doppler-broadened MB calculation that includes all the relevant atomic levels is a computationally intensive task. Instead we apply perturbation theory and calculate the lowest order response functions for both fields 3 and 4. We make the approximation that the pump fields 1 and 2 are constant, as field 1 is far from resonance and field 2 is not absorbed because there is little population in the $P_{1/2}$ level. We assume linear absorption/dispersion to be the dominant process for field 4. Given these assumptions, we may solve the wave equation for E_4 and get

$$E_4(z) = E_4(0)\mathrm{e}^{\alpha\bar{\chi}_1 z} \, . \tag{2.19}$$

Here $\alpha = 2\pi k_4 \tilde{\mu}_{da}^2 N/\hbar$ and $\bar{\chi}_1$ is the Doppler averaged linear response function which includes all relevant structure of the $5P_{3/2}$ excited and $F = 3$ $5S_{1/2}$ ground states. Here $\tilde{\mu}_{da} = \langle \alpha' L' \, || r || \, \alpha L \rangle$ is the reduced dipole matrix element. All the six-J and three-J symbols have been absorbed into the definition of χ_1. We consider only phase matched emission into field 3 and insert the result into the wave equation, yielding

$$\partial_z E_3 = \kappa \bar{\chi}_3 E_4^* \, , \tag{2.20}$$

where $\kappa = 2\pi k_3 \tilde{\mu}_{dc} \tilde{\mu}_{ad} \tilde{\mu}_{ba} \tilde{\mu}_{cb} N E_1 E_2/\hbar^3$ and $\bar{\chi}_3$ is the Doppler broadened non-linear

susceptibility which takes all relevant atomic structure into account (see next section). Again the tilde denotes reduced dipole moments. The numerical values for these are $\tilde{\mu}_{ba} = \tilde{\mu}_{da} \approx 5.2\ ea_o$ and $\tilde{\mu}_{cb} = \tilde{\mu}_{cd} \approx 5.2\ ea_o$. We solve this simple differential equation subject to the boundary condition $E_3(0) = 0$ and get

$$E_3(z) = \frac{\kappa\bar{\chi}_3}{\alpha\bar{\chi}_1^*} E_4(0) \left(\mathrm{e}^{\alpha\bar{\chi}_1^* z} - 1\right) \ . \tag{2.21}$$

In the limit that the interaction region (the cell) is much longer than the characteristic absorption length of field 4, we can take $z \to \infty$. The exponential in equation 2.21 then goes to zero and the efficiency becomes

$$\mathcal{E} = \left(\frac{\kappa}{\alpha}\right)^2 \left|\frac{\bar{\chi}_3}{\bar{\chi}_1}\right|^2 = \left(\frac{k_3}{k_4} \frac{\mu_{dc}\mu_{ba}\mu_{cb}}{\hbar^2 \mu_{da}} E_1 E_2\right)^2 \left|\frac{\bar{\chi}_3}{\bar{\chi}_1}\right|^2 \ . \tag{2.22}$$

Notice that the atomic density, N, is absent. This comes about because of the assumption that all the 780 nm photons are absorbed. To apply Eq. 2.22 to a Doppler free medium such as an ensemble of cold atoms, one could drop the bars on the response functions, giving a closed form solution. We have checked that the MB result agrees with Eq. 2.22 when we restrict the perturbative treatment to the simple 4-level atomic structure.

We do not know of a simple form for the inhomogeneously broadened response functions so we numerically integrate them. For parameters similar to those in the experiment we see a peak theoretical efficiency of 2×10^{-5}. This theoretical efficiency is of the same order as the experimental efficiency, which is reasonable, given the number of approximations we are making (*e.g.* perturbative response functions, linear absorption, undepleted pumps, plane wave fields). Clearly, the conversion efficiency of 780 nm light to 1367 nm light is limited by the linear absorption of the

medium. One may consider using electro-magnetically induced transparency (EIT) to possibly increase the 4WM efficiency [22].

2.5.4.1 Calculation of the Susceptibilities

We present how we calculate the suceptibilities, χ_1 and χ_3, used in Eqs 2.19-2.22. To calculate χ_1 we use the fact that the 780 nm laser, or field 4, is resonant with the $5S_{1/2}$ F=3 ground state to the $5P_{3/2}$ F=4 excited state and ignore the other F=2 ground state manifold. Atoms that are Doppler shifted into resonance with the $5P_{3/2}$ F=3 and F=2 states contribute to the absorption, so we keep those states as well. We assume linearly polarized light along the $\hat{x}$ direction and all field propogation along $\hat{z}$. Summing over all allowed transitions between magnetic sub-levels and averaging over the initial states gives us

$$\chi_1 = \frac{i}{12}\left(\frac{1}{\delta_4} + \frac{35}{81}\frac{1}{\delta_3} + \frac{10}{81}\frac{1}{\delta_2}\right) . \tag{2.23}$$

Here $\delta_j = \Delta_{d_j a_3} - i\Gamma_{d_j a_3}$. The state labels (*e.g.* d_4) refer to hyperfine states indicted in Fig. 2.1 and the subscripts indicate the F sub-level.

We again only consider the F=3 portion of the ground state manifold for the calculation of χ_3. Because the 795 laser is far detuned from the $5P_{3/2}$ states we must keep both the contribution from the F=2 and F=3 hyperfine states. In the experiment the 795 nm and 1324 nm lasers are tuned to two-photon resonance with the $6S_{1/2}$ F=3 manifold, thus we can ignore the F=2 upper state. From Fig. 2.4 it is clear that the 4WM process is strongest through the $5P_{3/2}$ F=4 states so we keep only terms involving that state and disregard the contributions from the rest

of the D2 line. Fields 1 and 2 are taken to be polarized in the $\hat{y}$ direction while field 4 is polarized along $\hat{x}$. This choice of polarization forces the generated field 3 to be polarized along $\hat{x}$ as well. The result is

$$\begin{aligned} \chi_3 &= \frac{i}{12}\frac{1}{18}\frac{1}{(\Delta_{d_4a_3}+i\Gamma_{d_4a_3})(\Delta_{c_3a_3}-i\Gamma_{c_3a_3})} \\ &\times \left[\frac{1}{(\Delta_{b_3a_3}-i\Gamma_{b_3a_3})}+\frac{1}{(\Delta_{b_2a_3}-i\Gamma_{b_2a_3})}\right]. \end{aligned} \tag{2.24}$$

We arrive at the Doppler broadened response functions following the prescription of Eq. 2.14.

We look at the transmission of the 4WM cell experimentally and compare it to the form given by Eqs. 2.23. Figure 2.9 shows the transmission of a weak 780 nm probe beam at several different cell temperatures along with a fit using the linear response function shown above with the temperature as the only free parameter. We can extract the optical depth from the model and see that it is as high as 80 for the hottest cell temperature. According to Fig. 2.9f the measured cell temperature and the one we get from the model are consistently off by more than 10 °C. This systematic problem can be related to inappropriate thermal contact between the sensor and the cell, or to other equipment problems. We do not preclude that the simple model that we use is insufficient to capture the whole dynamics of the multilevel atoms.

2.6 Conclusion

We have observed 4WM in the diamond configuration in a warm atomic ensemble of rubidium. We have observed narrow features in the 4WM gain that arise

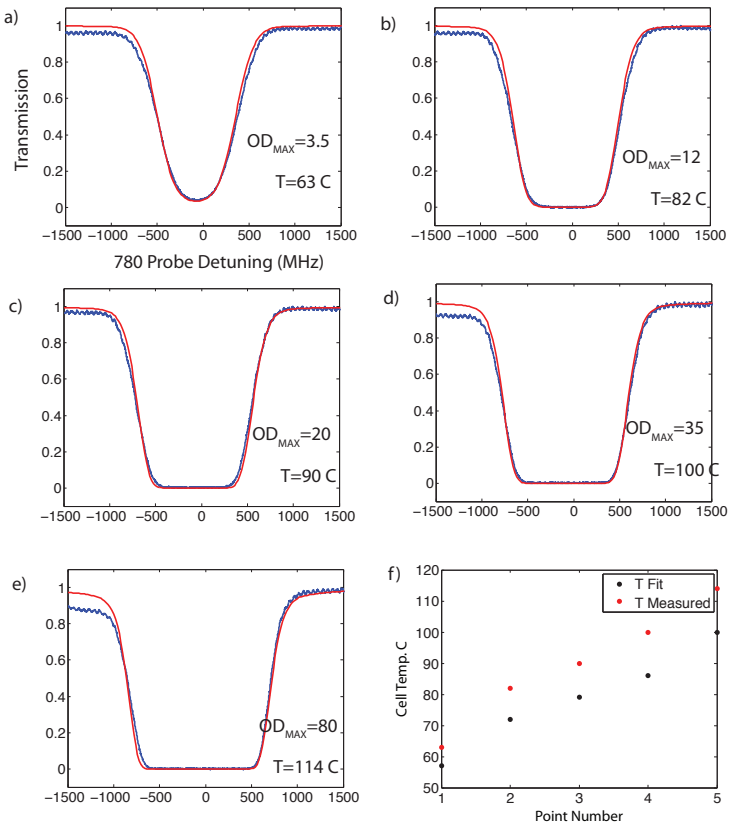

Figure 2.9: The transmission of a weak probe 780 nm laser through the 4WM cell at different cell temperatures a)-e). Both the model (red) and the data (blue) are on each plot. f) The measured temperature of the cell compared to the one derived from the fit.

from velocity-class selective resonant enhancement. When using strong resonant pumps we observe Autler-Townes style splitting in the 4WM resonance structure. We have measured the efficiency of the 4WM process and have shown it to be low, on the order of 10^{-4} due to the linear absorption of the pump beam. In the rest of this thesis we will consider pair generation from the ensemble but the knowledge we gained in the semiclassical regime will aid us in understanding the quantum mechanical system.

Chapter 3

Pair Production From a Warm Ensemble

3.1 Introduction

In this chapter we discuss measurements and theory regarding photon pair production from the warm atomic medium. The first section explains the experimental details unique to the photon counting measurements that are the subject of the remainder of this thesis. We discuss the temporal and spectral properties of the biphotons in two different regimes of pumping. Using a second Rb cell as a filter we measure the spectral character of the generated pairs. A simple theory involving a decaying three level atom and spectral filter gives qualitative agreement with some of the data.

Entangled pairs of photons are currently the only option for achieving long-distance secure quantum communication but suffer from loss in fiber optic channels. Duan *et al.*[26] suggested a method for overcoming this by inserting atomic ensemble-based quantum repeaters in the communication channel. An integral part of many of the schemes based on the ideas of Ref. [26] is a source of correlated photon pairs that are resonant with atomic quantum memories. Spontaneous four-wave mixing (4WM) in atomic ensembles is a well-suited candidate for this application [4, 53, 37], complimenting the work done in optical fibers [39]. Chaneliere *et al.* [17] proposed a quantum repeater that operates at telecommunication wavelengths

and experimentally demonstrated pair production from a laser-cooled, cold atomic ensemble with one photon in the telecommunications band and the other in the near-IR. Balic *et al.* [4] and Du *et al.* [25] have demonstrated biphoton generation in the near-IR with controllable correlation times.

Our current experimental effort focuses on frequency and temporal control of biphotons created in a warm atomic ensemble (isotopically pure ^{85}Rb) using a four wave mixing (4WM) interaction [5, 61]. The two correlated photons occur at different wavelengths, 1367 nm and 780 nm. We measure the polarization entanglement of the photons through a violation of Bell's inequality. The gain of the non-linear 4WM interaction and the linear absorption/dispersion of the medium determine the temporal and spectral character of the pairs. Changing the parameters of the pump lasers can modify both the gain and the absorption/dispersion of the medium. Spectral filtering and additional laser fields allow modification and control of the frequency and temporal properties of the biphotons. The control that we achieve is passive and opens the door to future active quantum feedback.

3.2 Photon counting experimental set up

3.2.1 Optical Setup

The optical setup is shown in Fig. 3.1. The setup is very similar to the one we used for the semiclassical measurements in chapter 2. We use the same angles, which are indicated again in the figure caption. The obvious difference is that for pair generation we remove the 780 nm pump beam. We couple both of the output

beams into appropriate single mode fibers. The 780 nm photon goes through a 1 meter fiber and then onto a silicon avalanche photodiode (APD). The 1367 nm photon goes thorough 200 m of fiber that serves to optically delay it by 1 μs and then onto the InGaAs APD.

To align the system we first put all three pump beams on the ensemble and maximize the generated 4WM light. We then optimize the coupling of the 4WM light into its fiber. We can achieve up to 70% coupling of the 4WM into the single mode fiber. We also couple the 780 nm pump beam into single mode fiber with a maximum efficiency of 80%. Then, in a final alignment step, we remove the 780 nm pump and observe and maximize the pair coincidence rate.

3.2.2 The Detectors

We use two different types of detectors in the experiment. Both detectors are single photon counting APDs. The detector used for the 780 nm photons is a Silicon based EG&G SPCM (now made by Perkin Elmer). The detector is free-running, meaning it is always on except for a 30 ns dead time after registering a count. The detection efficiency of the detector is $\approx$ 40% and the dark count rate is $\approx$ 200 counts/s.

The detector for the 1367 nm photons is an InGaAs APD from Princeton Lightwave. The detector must be run in gated mode due to the high dark count rate. Given a triggering pulse the detector is gated on for a 1 ns window at a maximum rate of 20 MHz. Due to the large probability of after pulsing the blanking may be set

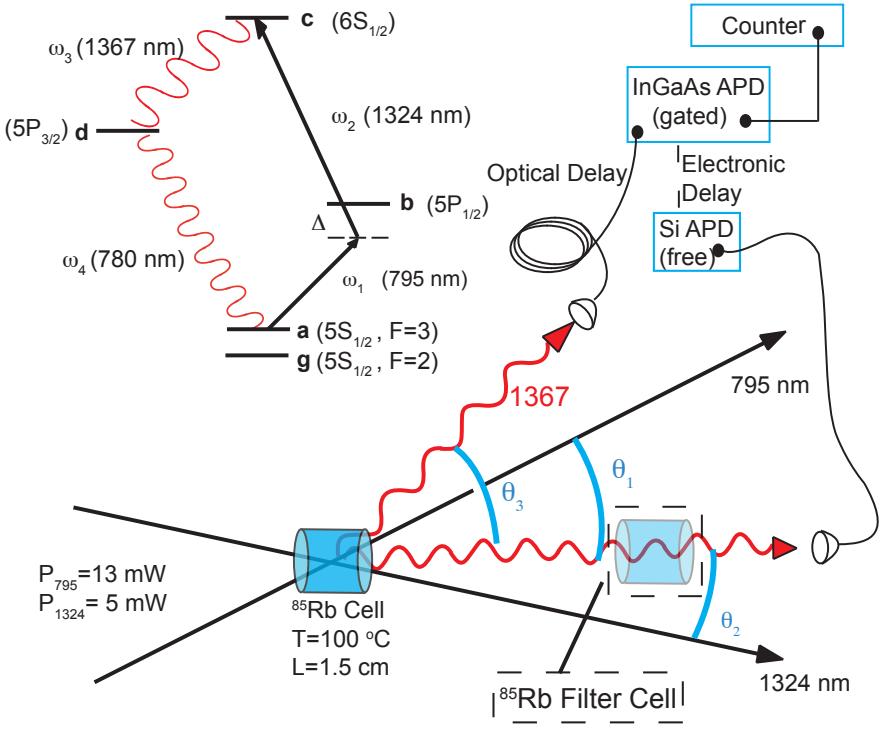

Figure 3.1: A schematic of the experimental apparatus and a simplified energy level structure. The angles defining the beam directions (not to scale in the picture) are $\theta_1 = 2.0°$, $\theta_2 = 0.7°$, and $\theta_3 = 2.7°$.

to ignore a number of triggering pulses immediately after a count. The dark count probability in each 1 ns gate is 3×10^{-6}. The specification from the manufacturer for the efficiency of the detector is 20%. Our measurements of the detector efficiency have given a values ranging from $10 - 15\%$.

3.2.3 Counting Electronics

Figure 3.2 shows a detailed diagram of the counting electronics. The 780 nm photon is incident on a EG&G SPCM silicon APD which emits a 40 ns pulse upon registering a photon. The pulse is sent to the trigger input of the SRS DG353 delay generator and to channel A of a SRS SR400 photon counter which counts the pulses. The delay generator upon receiving a trigger sends a pulse to the triggering input of the InGaAs APD after a programmable delay. During that time the 1367 nm photon has been in the optical delay line fiber. When the programmable delay is set properly the 1367 photon arrives on the InGaAs APD at the same time as the detector is triggered on and an output pulse is sent to channel B of the SR400 photon counter. The delay is controlled by a Labview program via GPIB and the data is recorded by the computer. Therefore, to take a cross-correlation function, the computer fixes the delay and then records the number of counts after some fixed integration time, then changes the delay and integrates again.

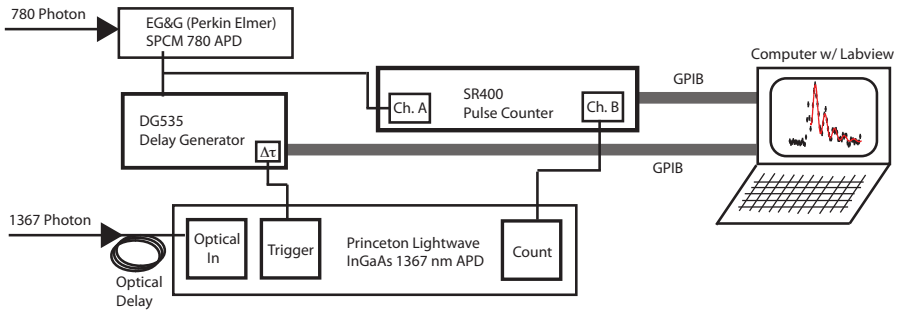

Figure 3.2: A detailed diagram of the counting electronics for obtaining the cross-correlation function. See the text.

3.3 Pair Creation From Spontaneous 4WM

Here we describe the physical mechanism which leads to pair creation from the medium. A full theory for the process is quite involved. The theory must take into account propagation, linear absorption, 4WM gain, spontaneous emission/atomic lifetimes, and phase matching considerations. It is possible to write down the Hamiltonian of the system and to develop Heisenberg-Langevein equations for the atomic and photonic operators [40, 36]. Then using a C-number treatment and methods from stochastic differential equations, solve for measured quantities like second order correlation functions [14, 15]. We instead use a simplified theoretical model to help understand the generation process.

The process is very similar to semi-classical 4WM but in place of a third pump beam, the generation is seeded by vacuum fluctuation. Two pump beams, at 795 nm and 1324 nm, give rise to a spontaneously generated 1367 nm photon which is emitted into 4π with a dipole radiation pattern. If we let $\vec{k}_3$ denote the k-vector of

the 1367 nm then upon emission of the photon the medium is left in the excited state $|\psi\rangle = \sum_i \exp(i\phi_i)\,|d_i a_{else}\rangle$ with a spatially varying phase $\phi_i = \vec{r_i} \cdot \left(\vec{k}_1 + \vec{k}_2 - \vec{k}_3\right)$. The sum here is over all atoms in the sample and a and d are the atomic state labels consistent with our usual convention. Since there is no measurement that specifies which atom emitted the photon, the excitation is shared among all the atoms. The 780 nm photon is then emitted in the phase-matched direction due to constructive interference. In this situation correlated pairs actually occur on opposite sides of two concentric rings. In the experiment we choose to observe those that occur co-planar with the pumping beams.

3.4 The Cross-Correlation Function

In this section we examine the cross-correlation of the pair of photons for several different pumping parameters. We measure the spectral character of the photons and show that by changing pump laser parameters we may modify the temporal profile of the photons.

3.4.1 Off-Resonant Pumping

Figure 3.3 shows a typical measured cross-correlation function with the 795 nm pump laser detuned $\Delta = 1.5$ GHz below the $5S_{1/2}$ F=3 $\rightarrow$ $5P_{1/2}$ F=2 transition, well outside the Doppler width. The 1324-nm pump laser frequency closes the $5S_{1/2}$ F=3 $\rightarrow$ $6S_{1/2}$ F=3 two-photon transition in the level scheme of Fig. 3.1. The polarization analyzers for the signal beams pass vertically polarized photons. The width of the

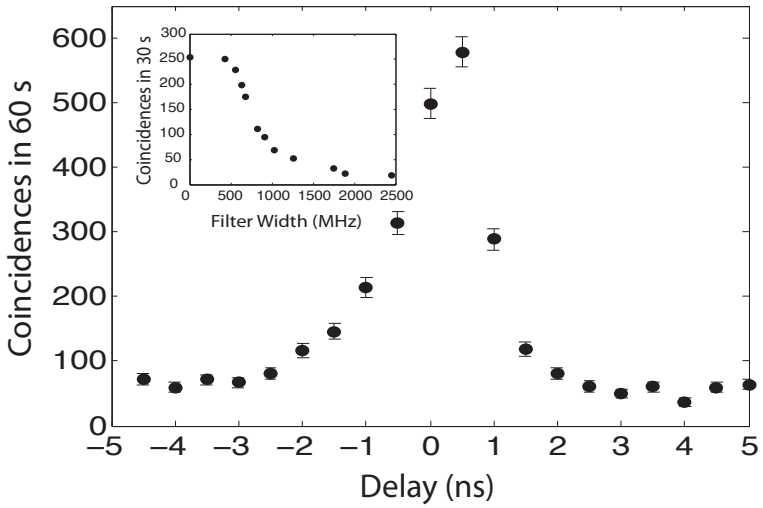

Figure 3.3: Cross-correlation function for a 1.5 GHz red-detuned 795 nm pump and no filter cell. Inset: Coincidence counts at zero delay as a function of the ^{85}Rb cell filter spectral width.

correlation function is surprisingly short ($\approx 1-2$ ns), on the order of the resolution of the detector (which at best is the 1 ns gat width of the InGaAs APD), rather than of order the lifetime of the intermediate $5P_{3/2}$ state as might be expected.

3.4.2 Filter Cell

To understand the temporal and spectral character of the correlated pairs, we insert a 7 cm hot rubidium cell into the path of the 780-nm photons as illustrated in Fig. 3.1 to act as a filter. Ideally we would use a variable narrow band interference filter, however commercial filters have bandwidths on the order of 1 nm, which is much too large for our application. A Fabry-Perot filter is a viable option but is more complicated to implement than the Rb cell filter. We record coincidence counts

at zero delay and vary the temperature of the filter cell, changing the width of the transmission region. Figure 3.4a shows the filter cell transmission for a weak 780 nm probe beam for several temperatures as well as the transmission through the 4WM cell. Figure 3.4b shows the coincidences in 30 s as a function of the filter width (50% transmission). No change in the coincidence rate occurs until the filter cell absorption is wider than that of the 4WM cell, implying that the correlated photon pairs occur predominantly far detuned from the intermediate state resonance. The 4WM cell optical depth for resonant 780-nm photons can be very high as we saw in chapter 2, so the large majority of biphotons generated near resonance (as is expected from density matrix calculations) are re-scattered many times and do not reach the detectors, time-correlated in the phase matched direction. The photons that emerge from the cell are detuned from the intermediate resonance (level d in Fig. 3.1) and this gives rise to the short correlation time. The measurement of the transmission as a function of filter width gives a bandwidth of the 780 nm component of the biphoton of approximately 350 MHz. Note this is in contrast to Ref. [17], which observed long (> 15 ns) correlation times from a laser-cooled sample. In this case the absence of Doppler broadening allows photons much closer to resonance to be transmitted, and thus longer correlation times.

3.4.3 Resonant Pumping

If we vary the frequency of the pump lasers, the cross-correlation function changes. With the 795-nm pump laser set close to the $5S_{1/2}$ F=3 $\rightarrow$ $5P_{1/2}$ F=2

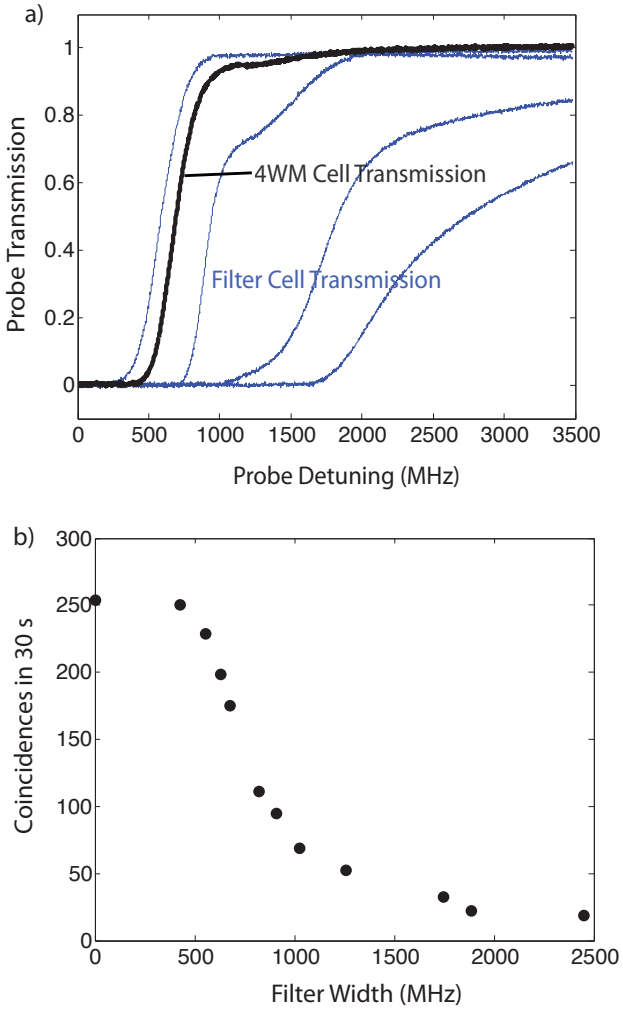

Figure 3.4: a) The transmission of a weak 780 nm probe beam through the 4WM cell and the filter cell at different temperatures. b) The number of coincidences for different width filters.

transition and the 1324-nm pump laser 100 MHz above of the two-photon, zero-velocity class resonance (see Fig. 3.5a), the correlation function shows two distinct features. The narrow peak at zero delay is similar to the one shown the previous off-reosnant pump case (Fig. 3.3), while the second feature shows a longer decay with oscillations, attributable to quantum beats.

The Fourier transform of the correlation shows a peak at approximately 120 MHz, consistent with the hyperfine splitting between the $F = 3$ and $F = 4$ of the $5P_{3/2}$ ^{85}Rb excited state. Multiple decay paths exist due to the hyperfine splitting of the intermediate state [1, 17]. The choice of the F sublevel in the initial state allows decay through a different intermediate path that shows different interval frequencies. Additional measurements with a ^{87}Rb atomic sample also show quantum beats at the appropriate hyperfine intervals of that isotope. The continuous (red) line in Fig. 3.5a) is a fit to the data from 3-45 ns to an exponentially decaying sinusoid with a frequency equal to the relevant hyperfine splitting of $f = 120.6$ MHz. We find a decay constant of $\tau = 11.6(2)$ ns with a reduced χ^2 of 1.9. This decay is shorter than the intermediate state lifetime of 26 ns. We will discuss this in more detail below.

The 4WM process does not provide any reason why varying the pump laser frequencies should modify the spontaneous cascade decay or the cross-correlation function. However, strong optical pumping due to the on-resonant 795-nm pump beam can change the population between the two ground state levels, including modifying particular velocity classes of atoms. Using the filter cell, we find that the narrow structure observed in Fig. 3.5(a) arises from far off-resonant photons while

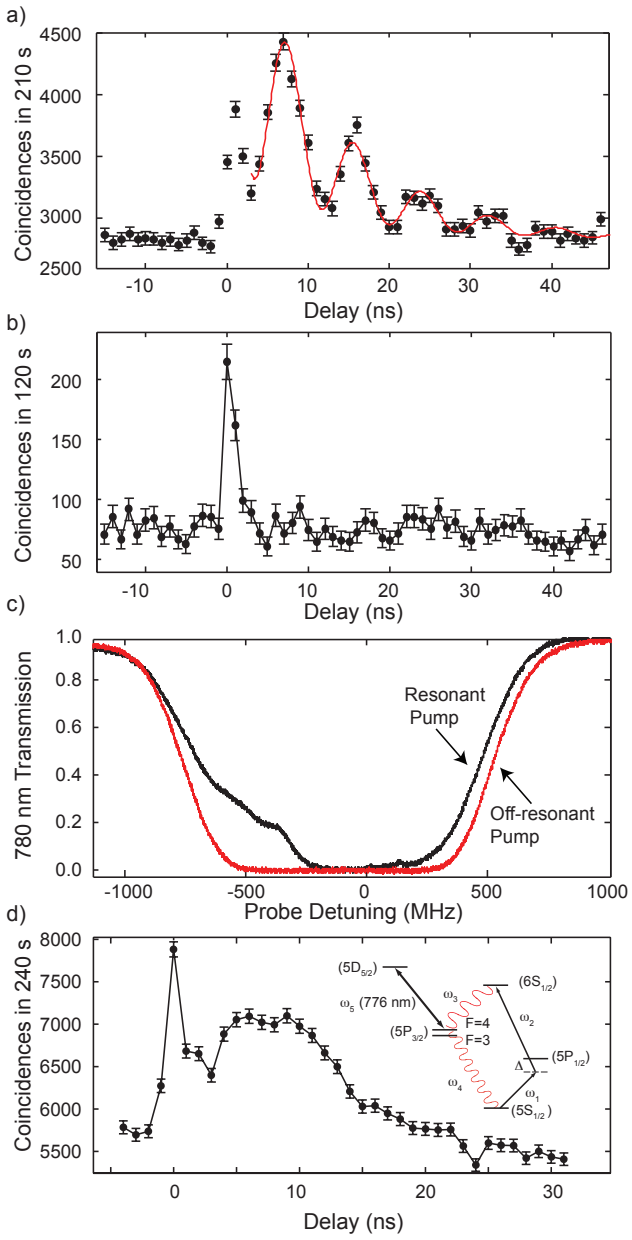

Figure 3.5: (a) Cross-correlation function with a resonant 795 nm pump beam, the red curve is a decaying oscillation at the hyperfine interval. (b) The cross-correlation function with a ^{85}Rb filter cell (same temperature as 4WM cell) in the 780-nm beam path. (c) The transmission of a weak 780-nm probe beam in the 4WM cell and the 4WM cell with resonant 795-nm pump laser. (d) Cross-correlation as in (a) except that a laser at 776 nm couples one of the hyperfine levels of the $5P_{3/2}$ state out of the diamond as shown in the inset. The solid lines in (b) and (d) are guides for the eye.

the longer time structure occurs due to near-resonant photons transmitted due to a modified absorption profile (Fig. 3.5(b)). Fig. 3.5(c) shows the transmission of a weak 780-nm probe beam through the 4WM cell with and without the resonant 795 nm pump beam, showing the modification of the 4WM cell transmission of 780-nm light due to optical pumping. We do not have a complete model of the optical pumping to quantitatively compare to the transmission or correlation functions due to the complex nature of the many levels in the Doppler-broadened medium.

We note that in [25] and [24] the authors observe a similar narrow feature to what we observe in Fig. 3.5(a), which they attribute phenomena of the Sommerfeld-Brillouin precursor [27] [34] at the single-photon level. We have experimentally shown that the narrow feature arises from photons off resonance from the intermediate state. This provides a simple and direct explanation for the existence of an optical precursor.

3.4.4 Erasing the Quantum Beats

If we add another laser at 776 nm that connects only one of the hyperfine states in the $5P_{3/2}$ to the $5D_{5/2}$ we suppress the oscillation, gaining control over the temporal evolution of the correlation. This external field takes one part of the atomic wavefunction out of the diamond. Fig. 3.5(d) shows the correlation function without the time oscillations. The inset shows the energy levels involved in this controlled modification of the temporal evolution of the biphoton.

3.5 Filter Cell Model

We developed a qualitative model to understand the absorption in the 4WM cell and the subsequent modification of the corss-correlation function. A single three-level cascade atom, initially in the the excited state, decays and emits two photons in the process. The photons emitted on the upper and lower transitions are labeled 1 and 2, respectively. The two photons are incident on two separate detectors. We place a dispersive filter (simulating absorption in the 4WM cell) in front of detector 2 using the response of a warm sample of 2-level atoms resonant with the lower transition of the source atom. Mathematically the filter cell is represented by the filter function $f(\omega) = \exp(i\alpha\bar{\chi}(\omega))$ where α is a real constant involving the density and length of the sample and $\bar{\chi}(\omega)$ is the Doppler broadened linear response function for the 2-level filter atoms. The rate of coincidences then is

$$R \propto \left| \left\langle 0|\hat{E}_1^+(t_1)\hat{E}_{2D}^+(t_2)|\psi\right\rangle \right|^2 . \tag{3.1}$$

Here $|\psi\rangle$ is the two-photon quantum state of the field from the decaying atom, $|0\rangle$ denotes the vacuum, and $\hat{E}_j^+$ are the positive frequency field operators at the two detectors [57]. The effect of the filter is to modify the field operator by $\hat{E}_{2D}^+(t) = \int \mathcal{F}(t-\tau)\hat{E}_2^+(\tau)d\tau$, where $\hat{E}_2^+(t)$ is the free-space field operator and $\mathcal{F}(t)$ is the time-domain representation of the filter function [28]. The field generated by the single decaying atom is an approximation to a biphoton generated somewhere in the ensemble, while the filter in the model is the optical path that the biphoton traverses in the 4WM cell. References [40, 36] present models with propagation that incorporated the parametric gain and linear absorption in similar configurations.

Figure 3.6(a) shows the calculated coincidence rate as a function of delay for three different optical depth (OD) filters. The correlation time scales inversely with OD. This explanation also applies to a cold atomic sample and might be an alternative explanation for density-dependent correlation times observed in [17] that were attributed to superradiance.

This model gives insight into the resonant data shown in Fig. 3.5. We calculate the response function for our atomic filter using the Doppler-broadened linear response of a V-system, driven strongly on one transition. This gives the standard EIT or Autler-Townes response function. The model is analogous to the current system since the 795 nm pump is resonant with the b→a transition (see Fig. 3.1) and we observe photons emitted on the d→a transition. Similar to the data presented in Fig. 3.5, Fig. 3.6(b) shows a narrow short time structure arising from frequency components of the biphoton wave-packet that are far detuned from intermediate-state resonance. The theoretical results also display a long-time feature associated with frequency components inside the transparency window. Higher optical depth leads to a greater delay of the long time peak which is expected in a slow light medium.

3.5.1 Details of the Calculation

We start with one cascade atom in the upper state at time $t = 0$. The level structure is indicated in figure 3.7a. We are interested in calculating the cross

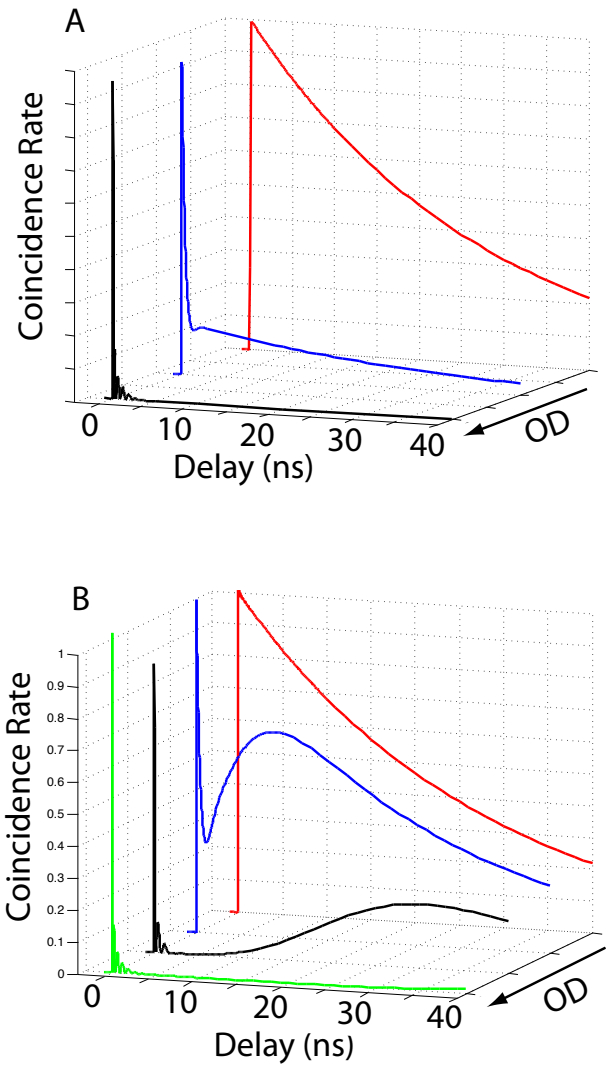

Figure 3.6: Theoretical prediction from the model described in the text for coincidence rates for (a) a simple hot cell of two level atoms and (b) a medium consisting of V-system atoms. In (a) it is clear that increasing optical depth leads to shorter time correlation functions.

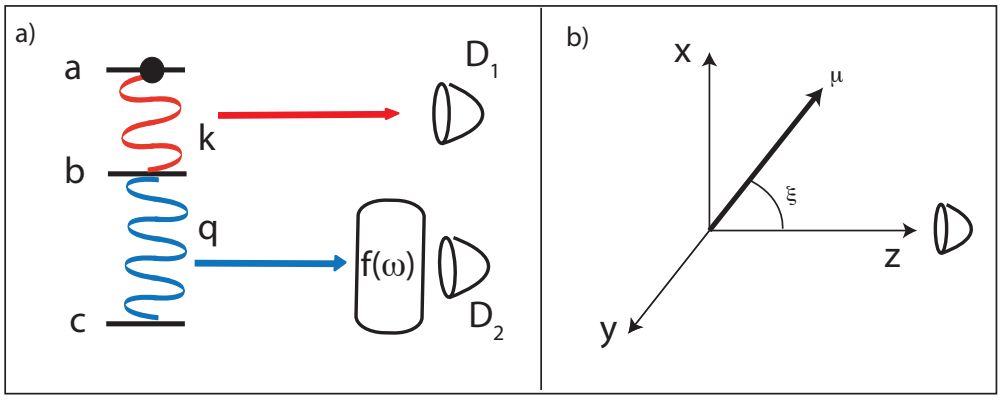

Figure 3.7: a) A schematic of the model. b) The geometry used for the angular integrations.

correlation function (CCF) or the coincidence rate. So the quantity to calculate is

$$|\Psi|^2 = \left|\left\langle 0 \left| E_k^+(t_1) E_q^{+D}(t_2) \right| \psi \right\rangle\right|^2 \ . \tag{3.2}$$

We assume the detectors are far from the atom and use the solution for the field emitted by a decaying cascade atom which is derived in Ref. [57],

$$|\psi\rangle = \sum_{k,q} -g_{a,k} g_{b,q} L_{kq} L_q \left|1_k, 1_q\right\rangle \ . \tag{3.3}$$

Here $L_{k,q} = \left[i(\nu_k + \nu_q - \omega_{ac}) - \frac{1}{2}\Gamma_a\right]^{-1}$ and $\left[L_q = i(\nu_q - \omega_{bc}) - \frac{1}{2}\Gamma_b\right]^{-1}$ and we have assumed the atom is at r=0. The g's are given by $g_k = -\vec{\mu}\cdot\hat{\epsilon}_k \mathcal{E}_k/\hbar$ where $\mathcal{E}_k = \sqrt{\frac{\hbar\nu_k}{2\epsilon_o V}}$.

The effect of the filter on the field operator at the detector is given by Ref. [28] as

$$E_q^{+D}(t) = \int_{-\infty}^{\infty} dt' \mathcal{F}(t - t') E_q^+(t') \ , \tag{3.4}$$

where $E_q^+ = \sum_{q,\lambda} \mathcal{E}_q \hat{\epsilon}_q^\lambda e^{-i\nu_q t + i\vec{q}\cdot\vec{r}} a_q^\lambda$. The field operator at the detector can be rewritten as

$$E_q^{+D} = \frac{V}{(2\pi)^3} \sum_\lambda \int d^3q \ \mathcal{E}_q \hat{\epsilon}_q^\lambda e^{-i\nu_q t + i\vec{q}\cdot\vec{r}} f(\nu_q) a_q^\lambda \ , \tag{3.5}$$

since $\mathcal{F}(t) = \int e^{-i\omega t} f(\omega) d\omega$.

We use the geometry in figure 3.7b where the detectors are both along the z direction and the dipole moments are in in the x-z plane. After taking care of the delta functions from the annihilation operators we get

$$\Psi(r_1, t_1, r_2, t_2) = \frac{V^2}{\hbar^2 (2\pi)^6} \int dk k^2 \int dq q^2 \mathcal{E}_k^2 \mathcal{E}_q^2 L_{kq} L_q e^{-i\nu_k t_1} e^{-i\nu_q t_2} f(\nu_q) \vec{\Theta}_k \vec{\Theta}_q \ , \quad (3.6)$$

where the Θ's are the angular integrals for k and q. These angular integrals are of the exact same form so we just need to look at one of them. The angular integral is

$$\Theta_k = \int d\phi_k \int d\theta_k \sin\theta_k \left(\sum_\lambda \vec{\mu}_{ab} \cdot \hat{\epsilon}_k^\lambda \hat{\epsilon}_k^\lambda \right) e^{i\vec{k}\cdot\vec{r}_1} \ . \quad (3.7)$$

We use a dyadic identity found in Scully [57](pg.313). The result is that in the far field only the x component is non-zero. The result is

$$\Theta_k = \hat{x} 2\pi \mu_{ab} \sin\eta \left(\frac{e^{ikr_1} - e^{-ikr_1}}{ikr_1} \right) \ . \quad (3.8)$$

We throw out the piece of 3.8 that goes like e^{-ikr_1} because it represents a wave propagating inward toward the origin. The resulting expression is

$$\Psi = \kappa \int d\nu_q \ \nu_q^2 f(\nu_q) e^{-i\nu_q t_2} e^{iqr_2} f(\nu_q) L_q \int d\nu_k \ \nu_k^2 e^{-i\nu_k t_1} e^{ikr_1} L_{kq} \ . \quad (3.9)$$

The k integral can be performed by contour integration, with the approximation that you may pull out the ν_k^2 from the integral (since it varies slowly over the region where the rest of the integrand is significant) and extend the lower limit of integration to $-\infty$ (since the integrand is negligible over that range). The end result is

$$\Psi = C\theta(\tau_1) e^{-i\tau_1\omega_{ac}} e^{-\frac{\Gamma_a}{2}\tau_1} \int d\nu_q \ \frac{e^{-i(\tau_2-\tau_1)\nu_q}}{i(\nu_q - \omega_{bc}) - \frac{1}{2}\Gamma_b} f(\nu_q) \ , \quad (3.10)$$

where $\tau_j = t_j - r_j/c$ and

$$C = \frac{1}{(2\pi)^2}\frac{1}{(2\epsilon_o)^2}\frac{\omega_{ab}^2\omega_{bc}^2}{c^6}\ \frac{\mu_{ab}\mu_{bc}\sin\eta_1\sin\eta_2}{|r_1|\ |r_2|}\ . \tag{3.11}$$

We are only interested in the time between the arrival of the two photons. This information is contained entirely in the remaining integral in Eqs. 3.10 which depends on the explicit form of the filter function $f(\nu_q)$.

The filter functions

To generate the results in Fig. 3.6 we use two different filter functions. In both cases we use that for the Fourier component of electric field at frequency ω propagating through a linear medium, $E_{out}(\omega)/E_{in}(\omega) = f(\omega) = e^{i\alpha\chi(\omega)}$. Now all that is left is to define the $\chi(\omega)$. The first case is for a gas of two level atoms. In this case, for atoms with the transition frequency ω_f.

$$\chi(\omega) = \frac{1}{\omega_f - \omega - \frac{i}{2}\Gamma_f} \tag{3.12}$$

To take into account the thermal motion of the filter atoms we then Doppler broaden the response function. The second filter function is for an atomic V-system with a strong resonant pump on one transition and the second transition with frequency ω_f which is close to the frequency of the photon emitted on the lower transition in our problem. The response function is them

$$\chi(\omega) = \frac{1}{\omega_{cb} - \omega - \frac{i}{2}\Gamma_{cb} - \frac{\Omega^2}{\omega_{cb}-\omega_{ab}-\omega-\frac{i}{2}\Gamma_{ca}}}\ , \tag{3.13}$$

which we then Doppler broaden appropriately.

3.6 The Decay Time of Correlations

We now turn to the decay time of the cross correlation function shown in Fig. 3.5(a) and (d). We measure a decay constant of $\tau \approx 12$ ns, less than half that of the intermediate state life-time of 26 ns. In Ref. [17] the authors observed a cross correlation that shortens with increasing optical depth, and attributed this behavior to super-radiance. In a double-Λ configuration [25] the cross correlation can be as long one μs due to slow light effects, which can be tuned by increasing the OD of the sample. We measure the correlation function at different atomic densities spanning two orders of magnitude, and find no change in the decay constant of the correlation function, in stark contrast to cold atom experiments.

A possible explanation of the insensitivity of the cross-correlation decay time to the OD in our warm sample is thermal diffusion. The two-photon excitation selects a relatively narrow velocity class of atoms with a width of velocities ($\Delta v \approx \Gamma_{2\gamma}/k_{2\gamma}$) creating a polarization grating that serves to scatter the generated 780 nm photon. Here $k_{2\gamma} = \left|\vec{k}_1 + \vec{k}_2\right|$ is the two-photon wave-vector and $\Gamma_{2\gamma}$ is a decay rate subject to power broadening. With classical 4WM [61], we have found $\Gamma_{2\gamma}/2\pi \sim 20$ MHz, which yields $\Delta v \approx 10$ m/s. Upon the emission of 1367-nm photon into the phase-matched direction a phased grating is established in the medium with a wavelength of 780 nm, which then decays due to diffusion, as within one intermediate state life time atoms with velocity Δv will move approximately 300 nm.

It is useful to consider N spatially phased classical dipole oscillators, which are perfectly phased at time t=0 to interfere constructively in the forward direction.

If those oscillators are then allowed to move ballistically with a Maxwell-Boltzman distribution with thermal velocity v_t, the intensity of the forward scattering has the form $I(t) \propto N + (N^2 - N) \exp\left[-\frac{1}{2}(kv_t t)^2\right]$. This form of exponential decay also applies to the forward emission of the 780 nm photon from the ensemble in our experimental case and therefore we expect a suppression of the correlation function with the functional form $\exp\left[-\frac{1}{2}(kv_t t)^2\right]$. We fit the data with the assumption that the correlation decays with a natural-linewidth decay time multiplied by an additional motional suppression factor. We find that the fit is as good in the reduced χ^2 sense as the fit without motional suppression. The thermal velocity from the fit for the data in Fig. 3.5c is $v_t = 6.6$ ms. With this modification, the model is in good qualitative agreement with the data.

3.7 Conclusion

We have experimentally demonstrated phase-matched emission of polarization entangled photons from a hot atomic ensemble. We have measured the structure of the time correlations in different regimes and showed that the temporal profile is determined in a large part by the dispersive and absorptive nature of the generation medium. We can control the spectral profile of the biphoton cross-correlation with a narrow band optical filter. We can also modify the temporal response by coupling a control laser that addresses a specific hyperfine transition. The production rate of entangled photons per unit bandwidth is comparable to other sources, but would be orders of magnitude larger if the absorption of the 780 nm photons could be

suppressed.

Chapter 4

Bell's Inequality, Photon Statistics, and Heralded Single Photons

Quantum optics disagrees with classical electromagnetic theory in some cases that can be realized rather easily in the laboratory with a correlated pair source. In the following sections we present three such cases. The first example is an experimental test of Bell's Inequality. Here we see that correlations in the polarization of two spatially separated photons is higher than that allowed classically. The second set of measurements shows a violation of the two beam Cauchy-Schwarz inequality. This result shows that the joint probability of photodetection at two different points is much higher than two detections at the same point, even when the average intensity is the same at both points. This is not possible classically [41]. In the last example, strong anti-correlation of photodetection events at the output ports of a beam splitter show the indivisible nature of the photon. In this measurement we look at our system as a source for heralded single photons and measure its performance.

4.1 Bell's Inequalitiy

In a very famous early paper on foundations of quantum mechanics Einstein, Podolsky, and Rosen [29] argued that the theory is not complete and brought to light the very peculiar non-local correlations predicted by quantum theory. Three decades later J. S. Bell, through very simple arguments, showed that any general

local hidden variable theory conflicted with quantum mechanics [6]. His work lead to the well known Bell's Inequality. If the inequality is violated then the system being interrogated cannot be described by a local theory. In the framework of quantum mechanics, violation of Bell's inequality proves the system is in an entangled state. Below we discuss Bell's inequality in terms of our experiment. We use the Clauser, Horne, Shimony, and Holt (CHSH) version of Bell's inequality derived in Ref. [20].

All tests to date have shown agreement between nature and quantum mechanics, which includes Bell's inequality. There are however loopholes in the experiments which have yet to all be closed at once. Disregarding the loopholes, Bell's inequality has been violated many times with many different systems. For photon pairs the list includes spontaneous emission from an atomic beam of atoms [30, 2], cold atom systems [17], and non-linear crystals using parametric down conversion [38]. Recently violations have been shown in trapped ions [43]. The data presented here is the first violation from a nonlinear interaction in an ensemble warm atoms.

Figure 4.1 shows a schematic for a typical Bell's inequality measurement based on the polarization of correlated photons. The photons, labeled A and B, emanate from a common source and head toward two detection setups. Before reaching the detectors each photon passes through a half-wave plate (HWP) and then onto a polarizing beam splitter (PBS) which passes horizontally polarized photons and reflects vertically polarized photons. The angle of the fast axis of the HWP relative to the horizontal at the two detection sites is denoted by a and b. At each site two detectors collect the photons that emerge from both the accepted port and rejected port of each PBS. We assign a measurement value of $+1$ when DA_+ or DB_+ registers

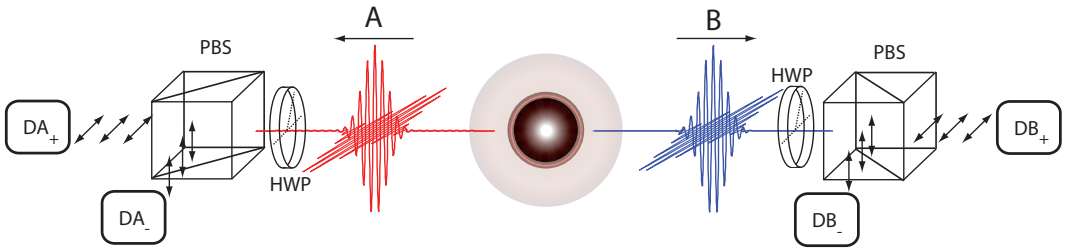

Figure 4.1: a) Schematic of Bell's inequality set up. Each photon is incident on a polarization analyzer and then onto single photon counting detectors.

a count and a value of -1 when DA_- or DB_- register a photon.

For a fixed setting of the polarizers, (a, b), we can make the measurement many times and then compute the correlation function of detection events at each site as

$$C(a,b) = \frac{N_{++} + N_{--} - N_{+-} - N_{-+}}{N_{++} + N_{--} + N_{+-} + N_{-+}} \,, \tag{4.1}$$

where N_{ij} is the number of times detector DA_i and DB_j registered a count in the same trial. Bell's inequality the can be written as

$$\mathcal{S} \equiv |C(a,b) - C(a,b')| + |C(a',b') + C(a',b)| \leq 2 \,. \tag{4.2}$$

Thus to check the inequality one must pick 4 polarizer settings (a, a', b, b') and count coincidences.

Before we get to the experimental results, simple quantum mechanical treatment shows what to expect. Each term in the correlation function $C(a, b)$ is just the probability of measuring a coincidence for a particular set of polarizer settings.

The probability of coincidence at DA_+ and DB_+ can be computed as

$$P(\theta_a, \theta_b) = |\langle H, H|U_{HWP}(\theta_a) \otimes U_{HWP}(\theta_b)|\Psi\rangle|^2 . \tag{4.3}$$

Here $|H, H\rangle$ is the ket representing photons A and B in the horizontal mode. The ket $|\Psi\rangle$ is the quantum state of the photon pair and U_{HWP} is the unitary matrix representing the action of the HWP on the photons such that the measurement at each site is to project the photon state onto $\langle H| U_{HWP}(\theta)$. Note that this has the effect of projecting the photon state onto the polarization state that is 2θ from the horizontal. Explicitly the matrix is

$$U_{HWP}(\theta) = \begin{pmatrix} \cos(2\theta) & \sin(2\theta) \\ \sin(2\theta) & -\cos(2\theta) \end{pmatrix} . \tag{4.4}$$

If we assume a state

$$|\Psi\rangle = \cos(\chi)\,|HH\rangle + e^{i\phi}\sin(\chi)\,|VV\rangle \tag{4.5}$$

then we can calculate the coincidence probability. If we make the simplification that $\phi = 0$ and $\chi = \pi/4$ then the probability has the form $P(\theta_a, \theta_b) = \frac{1}{2}\cos^2[2(\theta_a - \theta_b)]$. The correlation function also has a simple expression, $C(\theta_a, \theta_b) = \cos(\theta_a - \theta_b)$. The maximal violation of Bell's Inequality is found for the angles $\theta_a = 0$, $\theta'_a = 45°/2$, $\theta_b = 67.5°/2$, and $\theta'_b = 22.5°/2$. For these settings we see $\mathcal{S} = 2\sqrt{2} > 2$. This turns out to be the largest violation of the inequality possible quantum mechanically and it always turns out smaller in experiment.

The experimental situation is very similar to the one in Fig. 4.1 with the exception that we have only one detector per site, so in order to measure N_{--}, N_{+-},

and N_{-+}, we turn the wave plate such that is rotates the measurement basis by 90°. The pump lasers are set to the off resonance position as discussed in Ch. 2 and Ch. 3 with the 795 nm pump red-detuned 1.5 GHz from the $5P_{1/2}$ D1 line and the 1324 nm laser set to close the two photon resonance. The powers in the beams are 5 mW in the 1324 nm laser and 13 mW in the 795 nm laser. The detector setup/counting electronics is identical to that used in the correlation function measurements in Ch. 3. We record coincidences at zero effective delay between the two photons for fixed polarizer settings. There is no explicit control of the magnetic environment of the cell.

Figure 4.2a shows the sinusoidal variation in the coincidence rate expected with one polarizer fixed as the other is rotated. For this data both pump lasers are horizontally polarized. Note from this point forward I will discuss angles in terms of the pass axis of the polarization analyzer and not the fast axis of the HWPs (There is a factor of two between them). In Fig. 4.2a we first fix the 1367 nm polarizer to pass horizontal ($\theta_a = 0$) and observe the curve shown in black. The curve is maximal at $\theta_b = 0°$ and reaches a minima around $\theta_b = 45°$ indicating that the state of the light is of the form considered in Eqs. 4.5. The two additional curves in Fig. 4.2a are taken with the 1367 nm polarizer set at $\pm 45°$. Using the expression for the coincidence detection probability with $\phi = 0$, but this time allowing χ to be free we see that $P(\theta_a = \pm 45°, \theta_b) = \frac{1}{2}\cos^2(\theta_b \mp \chi)$. This gives us a way of determining the value of χ which upon fitting is $\chi = -47.3 \pm 0.2°$. This is close to the state of equal superposition for which $\chi = 45°$ apart from the minus sign.

At the end of this subsection we calculate the polarization state of the photon

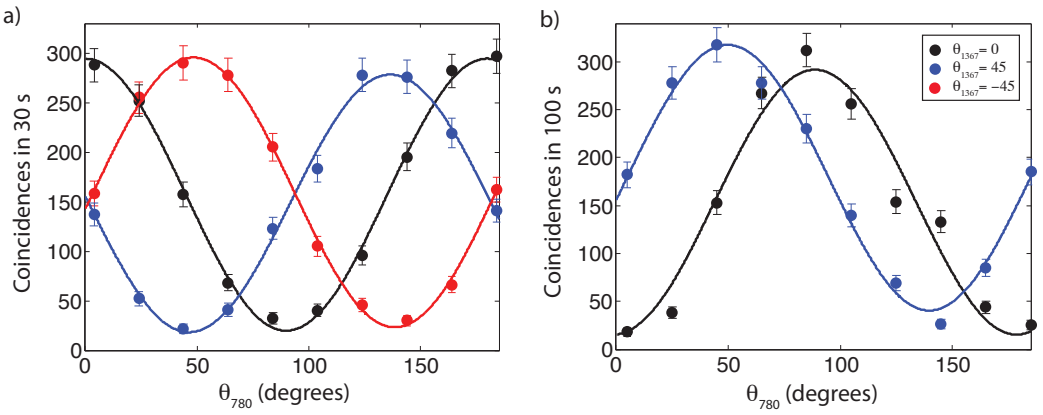

Figure 4.2: Sinusoidal variation in coincidence rate as a function of 780 nm polarizer setting. a) Coincidences for two horizontal pumps with the 1367 nm polarizer fixed at 0° and ±45°. b) Coincidences for one horizontal and one vertical pump with the 1367 nm polarizer fixed at 0° and 45°. Notice the difference in the two plots when $\theta_{1367} = 0°$.

pairs under the conditions above. We find that the predicted state is of the form of Eqs. 4.5 with $\chi = 45°$. There is a clear minus sign difference between the predicted and apparently measured state. The minus sign comes about due to a differential phase shift that the two polarization components (H and V) experience upon reflection from mirrors. In the beam path of the 780 nm photons before the polarization analyzer are two Thorlabs BE03 dielectric mirrors at near 45° incidence. The mirrors are made by multiple layers of dielectric with different indices of refraction and thus there can be non-trivial behavior in the phase shifts for transverse electric and transverse magnetic polarizations due to total internal reflection at the boundaries. However a measurement shows that the sum of the two mirrors is to accumulate effectively no total phase shift by the two mirrors. To measure the phase shift we put diagonally polarized light on the mirrors and look at what comes out on the

other side. A π phase shift results in anti-diagonal light. The 1367 nm photons are incident upon a single gold coated mirror before the polarizer. The same measurement shows that the single gold mirror applies a 180° phase shift between the H and V components of the 1367 nm polarization, which accounts for the sign difference between the theory and the experiment.

Figure 4.2b shows a similar situation to the one discussed above with one significant difference. In this example the 795 nm pump is vertically polarized while the 1324 nm pump is horizontally polarized. This time we see that with the 1367 nm polarizer set to pass horizontal ($\theta_a = 0$) the coincidence rate is at a minimum for $\theta_b = 0$. This shows that by changing the polarization of the pumps we are able to go from the Bell state $|HH\rangle \pm |VV\rangle$ to $|HV\rangle \pm |VH\rangle$.

We should note the the lack of perfect fidelity (the sine curves do not go all the way to zero) is an indication that the light field is not as simple as we are indicating. The dark count rate of the the detectors is too small to account for the offset of the curves. The major source of background in these measurements, as it is in all the correlation measurements in this thesis, is unpaired 1367 nm photons, presumably from pairs generated near resonance such that its partner 780 nm photon is rescattered in the generation medium. This background serves to suppress the value of the $\mathcal{S}$ parameter defined in Eqs. 4.2.

We next address the measurement of Bell's inequality. We integrate for 200 s at each of 16 polarizer settings, choosing to use the angles indicated above . The pump lasers are both horizontally polarized. The cell temperature is set to 365 K. We observe a convincing violation of Bell's inequality with $\mathcal{S}_{exp} = 2.22 \pm 0.03$. The

error is derived by assuming $\sqrt{N}$ Poissonian counting error. Thus we may say that the photon pairs produced by the source are polarization entangled. If we subtract off the uncorrelated background discussed above from all of the measurements we get a far stronger violation with $\mathcal{S}_{\text{fudged}} = 2.69 \pm 0.04$. There is no reason to subtract this background away since it arises from real photons, but does show how linear absorption of the 780 nm photons degrades the quality of the photon pair source.

Bell's State Calculation

Above we showed that with two horizontally polarized pumps the state in the experiment was very nearly the Bell state HH+VV once we take into account the changes in the polarization on the mirror reflections. Here we calculate what to expect for the polarization state of the emitted field from the spontaneous 4WM interaction. To do so we write down the Hamiltonian of the field interacting with a single atom including all the relevant hyperfine and Zeeman structure, and calculate the lowest order term in perturbation theory that contributes to the generation of phase matched photons. The single atom treatment of course does not give directional emission, as this is a multi-altom interference effect, but does predict the proper polarization state of the photon pairs.

We assume a single atom sitting at the origin pumped by two classical monochromatic $\hat{\pi}$ polarized plane wave pump beams. The pumps propagate in the $\hat{x}$ direction. The convention for the coordinate system appears in Fig. 4.3a. The emitted photons are represented by the field operators $\hat{a}_k^{(\lambda)}$ and $\hat{b}_q^{(\lambda)}$, where the λ denotes the two

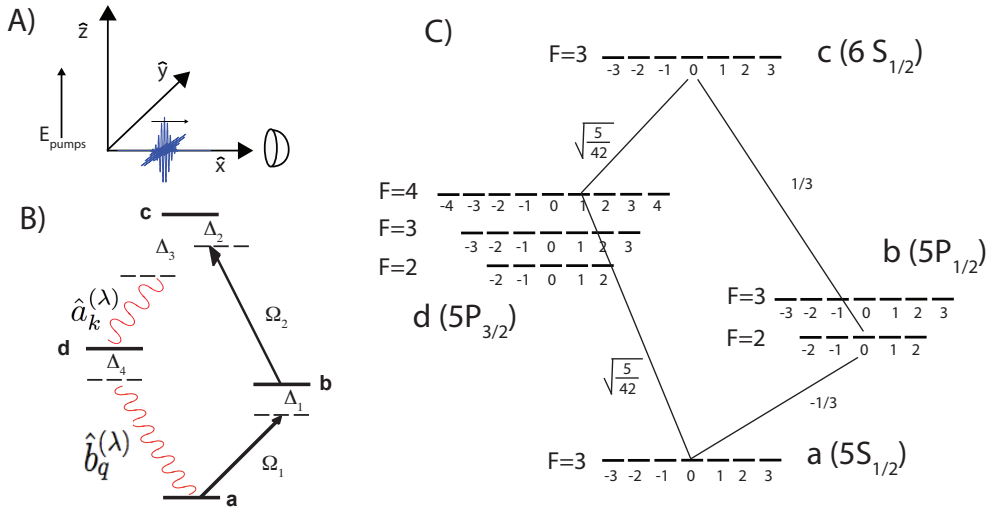

Figure 4.3: a) The geometry used in the calculation. The pumps are polarized along the z-axis and all fields propagate along the x-axis. b) The simplified level structure along with the coupling fields. c) The full level structure which is taken into account in the calculation. The lines show an example of a path out of the $m_F = 0$ ground state, along with the weights, that contributes to the 4WM.

polarization modes, which for the phase matched direction are horizontal $\equiv \hat{z} = \hat{u}_0$ and vertical $\equiv \hat{y} = \frac{i}{\sqrt{2}}(\hat{u}_{+1} + \hat{u}_{-1})$. We follow the conventions of Ref. [46] when it comes to polarization and calculation of all Clebsch-Gordon coefficients needed for the calculation. The interaction Hamiltonian in the interaction picture is then

$$\begin{aligned} V_I &= \hbar \sum_{i,j} \Omega_1^{ij} \hat{\sigma}_{ba}^{ij} \mathrm{e}^{i\Delta_1^{ij} t} + \hbar \sum_{i,j} \Omega_2^{ij} \hat{\sigma}_{cb}^{ij} \mathrm{e}^{i\Delta_2^{ij} t} + \text{H.C.} \\ &\quad + \sum_k \sum_{i,j} {}^{(\lambda)} g_k^{ij} \hat{a}_k^{(\lambda)} \hat{\sigma}_{cd}^{ij} \mathrm{e}^{i\Delta_k^{ij} t} + \sum_q \sum_{i,j} {}^{(\lambda)} g_q^{ij} \hat{b}_q^{(\lambda)} \hat{\sigma}_{da}^{ij} \mathrm{e}^{i\Delta_q^{ij} t} + \text{H.C.} \end{aligned} \tag{4.6}$$

The term that corresponds to pair generation comes about at fourth order in perturbation theory. We only consider terms that contribute to pairs emitted into the $\hat{x}$ direction. We first take into account only one of the initial Zeeman sub-states, denoted by α. The total wave-function can be written as $|\psi\rangle = |0\ 0\ a\rangle + |\psi_{4WM}\rangle + |\psi_{\text{OTHER}}\rangle$. The result for the 4WM piece is

$$|\psi_{4WM}\rangle \propto \sum_{k,q} \sum_{\lambda,\gamma} \sum_{j,k,l} \Omega_1^{j\alpha} \Omega_2^{k,j}\ {}^{\lambda} g_k^{*lk}\ {}^{\gamma} g_q^{*\alpha l} \mathcal{W}_{\alpha jkl}(t) \hat{a}_k^{\dagger(\lambda)} \hat{b}_q^{\dagger(\gamma)} |0\ 0\ a\rangle \ . \tag{4.7}$$

Here the sums over k and q are over the frequencies of the generated photons. The λ and γ sums are over horizontal and vertical polarization. The j, k, l sums are over all the intermediate Zeeman structure. The expression in Eqs. 4.7 is sum of all terms formed by stepping around the diamond, following the selection rules for the appropriate polarization, and weighting each term by the appropriate Clebsh-Gordan coefficients. The $\mathcal{W}_{\alpha jkl}(t)$ factor involves the four time integrals of the fourth order term in the Dyson's Series which after integration has the form $\frac{1}{\delta_1 \delta_2 \delta_3 \delta_4}$ where the δ_i are various detunings which are the same for every term up to hyperfine splittings. We make the reasonable assumption that the pairs we observe

are far from intermediate resonance compared to the hyperfine splittings. Under this assumption we may pull the $\mathcal{W}_{\alpha jkl}(t)$ through the j, k, l and λ, γ sums. Since the measurements we make do not depend on frequency we can, for our current purpose, ignore the sums over k and q. Then the answer for a single initial sub-state is

$$|\psi_\alpha\rangle = \cos(\chi_\alpha)\,|HH\rangle + \sin(\chi_\alpha)\,|VV\rangle \ , \tag{4.8}$$

where $\cos(\chi_\alpha) \propto \sum_{j,k,l} \Omega_1^{j\alpha}\Omega_2^{k,j}\ {}^H g_k^{*lk}\ {}^H g_q^{*\alpha l}$. A similar equation exists for $\sin(\chi_\alpha)$ with H replaced by V. The coefficient for the HV and VH terms are zero for two horizontally polarized pumps. To take into account all of the Zeeman ground states we suppose that the atoms begin in an incoherent mixture and thus the resulting state must be described by a density matrix $\rho = \sum_\alpha p_\alpha\,|\psi_\alpha\rangle\,\langle\psi_\alpha|$.

The solution, after summing over all paths, is the same regardless of the initial Zeeman state. It is $\cos(\chi_\alpha) = \sin(\chi_\alpha) = \frac{1}{\sqrt{2}}$. This answer agrees with the measurements presented earlier in the chapter. It is interesting that since each ground state gives the same Bell state we expect a pure polarization state but this result hinges on the large detuning assumption. In an optically thick cold atomic sample the region of complete absorption would be comparable to a few linewidths (6 MHz). Thus the already shaky assumption of large detuning is invalid. In Ref. [**?**] the authors measured a non-symetric polarization state for photons generated from a cold ensemble as is expected from our analysis.

4.2 Cauchy-Schwarz Inequality

Another point at which classical and quantum optics diverge is the statistics of the measured fields. For a stationary time varying field one may measure the average intensity $\bar{I} = \langle I(t) \rangle$, the variance of the intensity $\sigma^2 = \left\langle (I(t) - \bar{I})^2 \right\rangle$, the autocorrelation $\langle I(t) I(t+\tau) \rangle$, or higher order correlations. Second order (in intensity) correlation functions are interesting for many reasons but particularly so because classical inequalities may be derived that are very general and are in conflict with predictions from quantum optics.

Here we will consider a situation in which electromagnetic radiation falls on two detectors at separate spatial points. Each detector measures the light intensity denoted by $I_1(t)$ and $I_2(t)$. Classically, the intensities may be considered as functions which are described probabilistically. This means that the average intensity may be written $\langle I_j(t) \rangle = \int I_j(t) P\left[I_j(t), t\right] dI_j(t)$. This integral has the interpretation that we are integrating over all possible realizations of $I_j(t)$ at a fixed t weighted by the probability of that realization. For a stationary field, $\langle I \rangle$ is independent of t. In a similar way one can write cross correlations as averages over different realizations of $I(t)$. Now for the cross correlation function we may apply the Cauchy-Schwarz inequality for random variables which immediately gives $\left| \langle I_1(t) I_2(t+\tau) \rangle \right|^2 \leq \langle I_1(t)^2 \rangle \langle I_2(t)^2 \rangle$. Using the regular definition for the normalized cross correlation function $g_2^{\text{cross}}(\tau) = \langle I_1(t) I_2(t+\tau) \rangle / \left(\langle I_1 \rangle \langle I_2 \rangle \right)$ and for the autocorrelation function $g_2(\tau) = \langle I(t) I(t+\tau) \rangle / \langle I \rangle^2$ we may write the standard form of

the two beam Cauchy-Schwarz inequality [54] as

$$\mathcal{R} \equiv \frac{\left[g_2^{\text{cross}}(\tau)\right]^2}{g_2^{(1)}(0)g_2^{(2)}(0)} < 1 \; . \tag{4.9}$$

Equation 4.9 is a direct result of the assumption that we can describe the electric field as a classical stochastic process with a well behaved probability density. Quantum mechanically the field is not always describable in this way. The optical equivalence theorem shows that measurements of a quantum field may be described by a quasi-probability distribution using the diagonal coherent state representation [41]. This quasi-probability distribution need not be well behaved (more singular than a delta-function) or positive and can thus lead to violations of 4.9. States that have this quality are called non-classical.

To compare measurements to the C-S inequality we must measure the auto-correlation of each beam as well as the cross correlation of the fields. We make our measurements with single photon counting APDs. The resolution we choose to use is set by the InGaAs APDs to be 1 ns. With such a detector we can measure the probability of detecting a photon in a single 1 ns time bin, say at detector 1, and call it P_1. If this probability is low we may relate the average intensity and P_1 by $\langle I_1 \rangle = \eta P_1$ where η takes into account the efficiency of the detector. A similar relationship exists for the correlation functions.

As a guide we consider the simplest model that has any resemblance to the current case, parametric down conversion (PDC). We consider a two-mode model with a monochromatic pump and calculate the state for a short interaction time (a

short down conversion crystal). The result is

$$|\psi\rangle = \sqrt{1-|\lambda|^2}\sum_{n=0}^{\infty}\lambda^n\,|n,n\rangle\ , \tag{4.10}$$

where $0 < |\lambda| < 1$ is the interaction parameter and the ket represents n photons in each of the two generated modes. For this simple example we see that the probability of having n photons in each mode is just $P_n = (1-|\lambda|^2)\,|\lambda|^{2n}$. We can calculate the autocorrelation of each mode at zero delay and see it is $g_2(0) = 2$, exactly what is expected from a thermal field. The result for the cross-correlation is $g_2^{\text{cross}} = 1 + \frac{1}{|\lambda|^2}$. Putting these together it is easy to see that for this simple model quantum mechanics predicts a violation of the Cauchy-Schwarz inequality.

The experimental set up is shown in Fig. 4.4a. A single detector at each site is replaced by two in order to defeat technical issues, namely dead time and after pulsing. We denote detectors for the 1367 nm photons as $I1$ and $I2$. Similarly, the detectors for the 780 nm photons are called $S1$ and $S2$. For the 1367 photons the detection efficiency of both detectors is $\approx 10\%$. The efficiency of the 780 nm photodiodes is $\approx 40\%$. For the measurements presented here the 4WM cell is held at 388 K. The pump lasers are tuned to the off resonance configuration discussed in the last section. The power in the 1324 nm beam is 5 mW.

For all the measurements presented here we insert a filter cell into the path of the 780 nm photons. Fig. 4.4b shows the transmission of a weak probe laser through the 4WM ensemble as well as through the filter cell. As discussed in chapter 3, 780 nm photons that are created by 4WM that are inside the Doppler broadened absorption of the generation cell will re-scatter and thus contribute to an uncorrelated

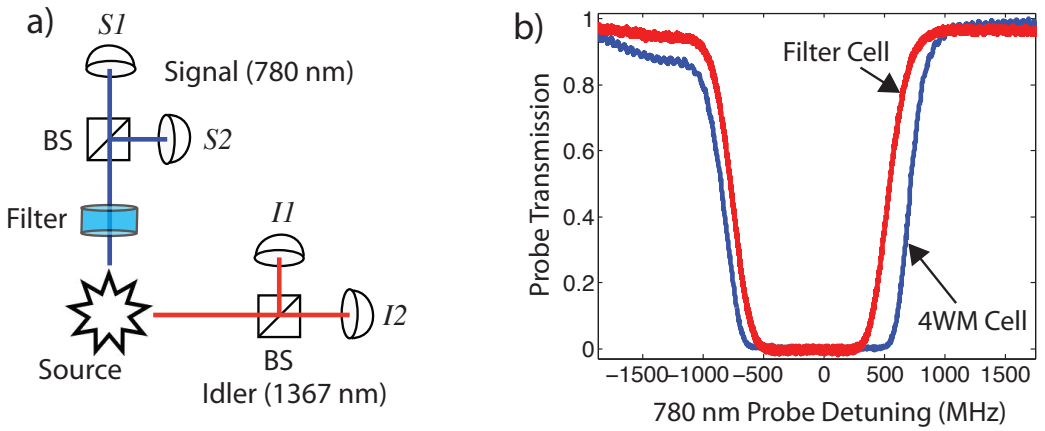

Figure 4.4: a) Schematic of the Cauchy-Schwarz inequality set up. Each photon is incident onto a 50/50 beamsplitter and then onto two single photon detectors. b) The transmission of a weak probe laser through the 4WM-cell ($T = 388$K) and through the filter cell ($T = 320$K).

background. We reduce the number of counts due to those photons rescattered photons with the filter cell.

Experimentally we measure the cross correlation function of the photon pairs $g_2^{\text{cross}}(\tau) = P_{I,S}(\tau)/(P_S P_I)$. Here P_S and P_I are the probabilities of receiving a count in any nanosecond time bin and $P_{I,S}(\tau)$ is the probability of detecting a signal and idler in two time bins separated by time τ. Figure 4.5(c) shows the unnormalized CCF. According to the data the biphoton has a temporal profile of approximately 1 ns. We see a peak raw coincidence rate of roughly 100 s^{-1} and an uncorrelated background of 4 s^{-1}. This ratio gives the maximum value of the normalized CCF to be $g_2^{\text{cross}}(0) = 27.2 \pm 1.3$. Taking into account detector efficiencies we observe a pair generation rate of 4,500 s^{-1}.

Figure 4.5 (a) shows the autocorrelation function for the 1367 nm light field

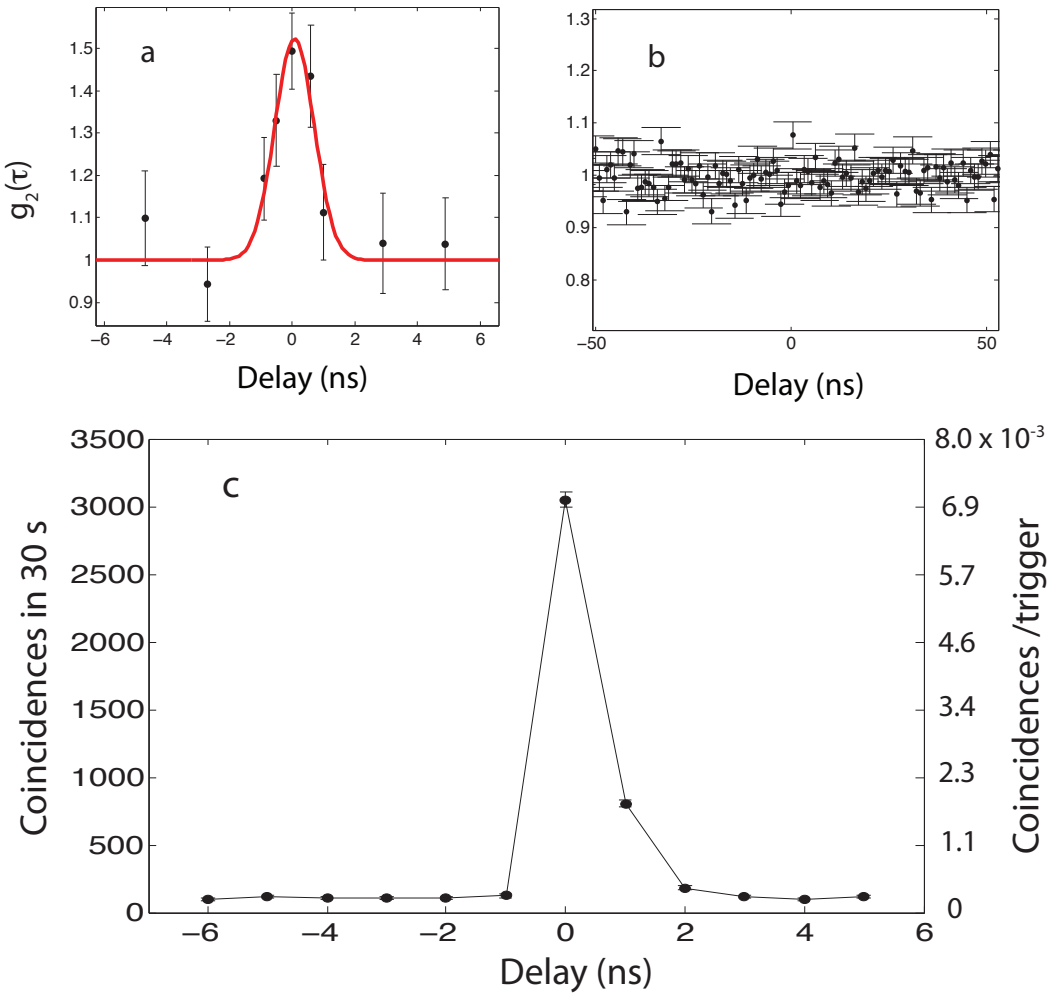

Figure 4.5: a) The normalized autocorrelation function of the 1367 nm light field. b) The autocorrelation function for the 780 nm light field. c) The cross correlation function for the two fields.

under the same pumping conditions indicated above. The measurement is performed by triggering both InGaAs APDs with a fixed delay between them at 7 MHz for 30 min per point. The output of the detectors is analyzed with a Field Programmable Gate Array (FPGA) circuit which records the number of singles and coincidences from detectors $I1$ and $I2$. The counting electronics set up is shown in Fig. 4.6. The delay is changed by adding different lengths of coaxial cable between the triggering source and the detectors. We see that the light is bunched, exactly as expected from light generated by a spontaneous process. For a perfect thermal source we would expect $g_2^I = 2$ [41]. The measured value at zero delay value is $g_2^I = 1.5 \pm 0.1$. It should be noted that we do not filter using polarization. In fact, for a perfect two polarization mode thermal source we expect $g_2^I = 1.5$.

Figure 4.5 (b) shows the observed autocorrelation for the 780 nm light field. Here, since the detectors are free running, we use a time stamper card (Becker & Hickl DPC-230) with a maximum resolution 164 ps to record arrival times for photons in detector $S1$ and $S2$. The correlation function is then calculated off-line. As in the earlier case we expect to see bunching in the g_2^S however it appears to be flat to the experimental uncertainty. Other measurements, performed at lower cell temperatures and thus lower optical depths, in the absence of the filter cell, do show bunching. We show the 780 nm autocorrelation at zero delay for 4 different temperatures in Fig. 4.7. It shows clearly the increase with lower temperature. A plausible explanation for this behavior is that in a very optically thick medium multiple scattering events cause frequency redistribution of the photons across the entire Doppler width, leading to a very narrow autocorrelation [47]. In Fig. 4.8a

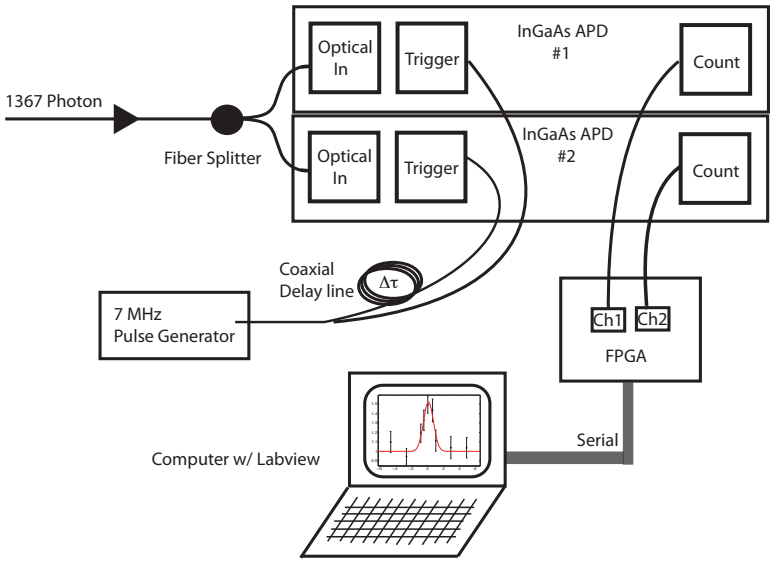

Figure 4.6: The electronics setup used to acquire the autocorrelation function of the 1367 nm photon field. Because the detectors must be run in a gated mode the most efficient way to collect the data was with a customized FPGA circuit. Different lengths of BNC cables change the relative delays.

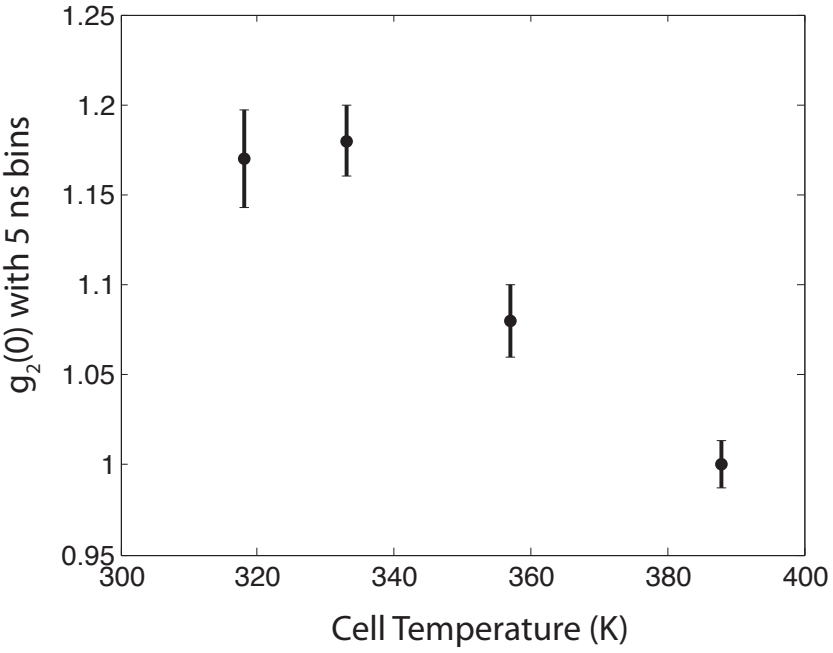

Figure 4.7: The autocorrelation function of the 780 nm photons at zero delay at different temperatures with 5 ns resolution.

we plot the autocorrelation function when the pump lasers are set to the resonant configuration. In this case the optical depth is reduced due to optical pumping and lower temperature ($T = 347$ K). Figure 4.8b shows $g_2(\tau)$ with the same laser parameters but with a polarizer in the beam, demonstrating the increase in correlation when we look at only one mode. At the 1 ns resolution and temperature used for the Cauchy-Schwarz inequality measurement, $g_2^S(0) = 1.0 \pm 0.1$.

We apply these measurements to the inequality in Eqs. 4.9. We observe a large violation with $\mathcal{R} = 495 \pm 56$, thus demonstrating that the light is strongly non-classical. This result compares favorably to results found in other warm atom systems where the authors observed violations but with $1 < \mathcal{R} < 2$ [18] . In cold

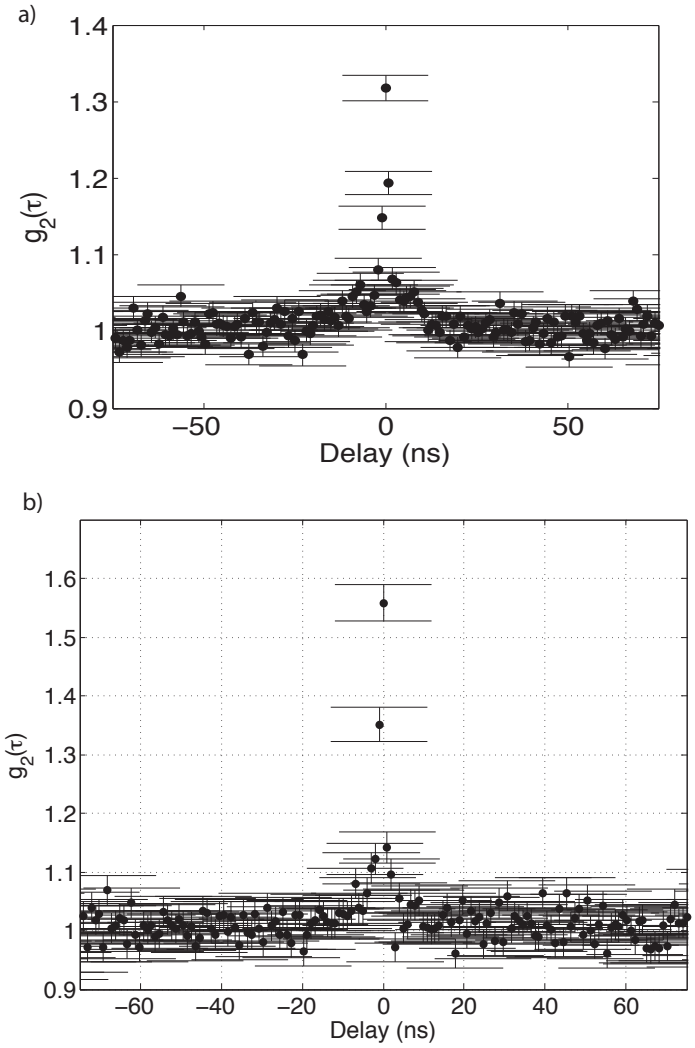

Figure 4.8: a) The autocorrelation function of the 780 nm field with resonant pumping and the 4WM cell at $T = 347$ K. b) Data taken under the same conditions as a) except with a polarizer in the beam path.

atoms with two photons at 795 nm $\mathcal{R} = 11,000$ has been observed [25]. Violation of the two beam Cauchy-Schwarz inequality has also been observed in the macroscopic regime using photocurrents from highly correlated bright beams [42]. Our result shows without a doubt that state of the biphoton, with very different wavelengths, cannot be described classically and the large violation shows the high degree of correlation between the fields.

4.3 Heralded Single Photons

Single photon states are non-classical by definition. Single photon states have applications to both quantum communication [7] as well as linear optical quantum computation. There are two main types of single photon sources. One produces single photons on demand, deterministically. The other, like the one discussed, here is a heralded source. For this type one waits for a signal to announce the presence of a photon. In our case we use a member of the correlated pair, the 780 nm photon, to herald the existence of a telecom-wavelenth 1367 nm photon. The quantities of interest for such a source are the generation rate, the heralding efficiency, the bandwidth of the photons, and how close the heralded state is to a single photon state.

The experimental measurement we make here is a conditional autocorrelation of the 1367 nm field. The setup is the same as shown in Fig 4.4a with the exception that we use only one detector for the 780 nm Signal photon. The idea is very simple, if upon receiving a herald 780 there is only one photon in the 1367 nm photon mode

then one and only one of the Idler detectors ($I1$ and $I2$) should register a count. Even in the ideal case where the state could be approximated by Eqs. 4.10, there is some finite probability of having more than one photon in each mode because multiple pairs could arrive simultaneously. Thus for stronger pumping we expect to have a higher probability for measuring two photons.

To quantify this we measure the conditional autocorrelation function

$$\tilde{g}_2^{\text{auto}}(0) = \frac{\tilde{P}_{I1,I2}(0)}{\tilde{P}_{I1}\tilde{P}_{I2}} \; . \tag{4.11}$$

Here the tilde denotes conditional quantities. Thus, $\tilde{P}_{I1}$ and $\tilde{P}_{I2}$ are the probabilities that a count occurs in detector $I1$ and $I2$, respectively, given that a 780 nm photon has been detected. The conditional probability that both detectors register a count at the same time is given by $\tilde{P}_{I1,I2}(0)$. Strictly speaking $\tilde{g}$ is a third order intensity correlation function for two 1367 photons and one 780 nm photon. For a perfect single photon state we would expect $\tilde{g}_2(0) = 0$. For the state of Eqs. 4.10 the conditional correlation function is $\tilde{g}_2(0) = 2\,|\lambda|^2$ which increases for larger interaction parameter. Here too, classical and quantum optics diverge. For a classical field it can be shown [33], again by the Cauchy-Schwarz inequality, that $\tilde{g}_2(0) \geq 1$ which is clearly violated by the example above.

Figure 4.9 shows the measured conditional autocorrelation function for different 795 nm pump powers. We see a decrease of coincidences of roughly a factor of 20 from a Poissonian source. At a pump power of 15 mW we see $\tilde{g}_2^{\text{auto}}(0) = 0.06$, a heralding efficiency of 10% and a HSP generation rate of 1500 s^{-1} (detector and filter efficiency corrected). The bandwidth of the photons, as shown in chapter 3,

is 350 MHz. The spectral brightness is thus 4.2 s^{-1}/MHz. For comparison, recent work in non-linear waveguides has shown conditional autocorrelations as low as 10^{-3} with heralding efficiencies of 50% and pair generation rates of 15 kHz. These sources, as well as those from parametric down conversion, typically have bandwidths around 1 nm determined by interference filters. Two specific examples from non-linear micro-structure fibers give spectral brightnesses of 0.7 s^{-1}/MHz [45] and 0.1 s^{-1}/MHz [32]. Placing the gain medium in a cavity can enhance the spectral brightness of a source. Brightnesses as high as 1,500 s^{-1}/MHz have been reported in cavity-enhanced parametric down-conversion [50] but require complicated frequency filtering.

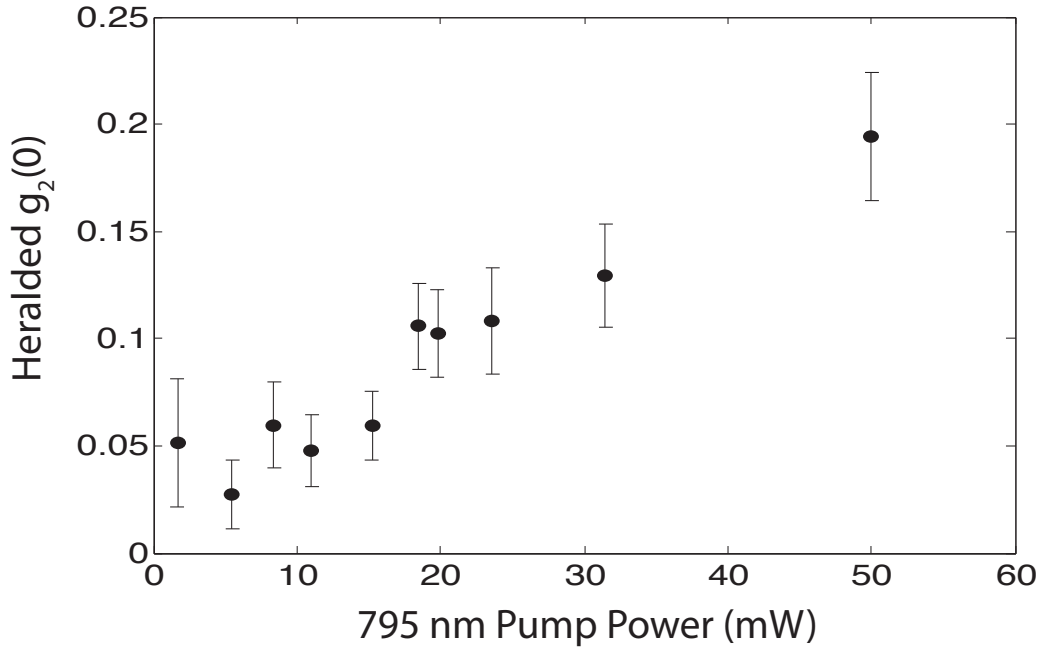

Figure 4.9: The conditional autocorrelation function of the 1367 nm field heralded by a 780 nm photodetection. Classically $\tilde{g}(0) > 1$ however we see that it is suppressed by a factor of 20.

Chapter 5

Concluding Remarks

We have demonstrated pair production from a hot atomic ensemble of rubidium using spontaneous 4WM. Using the diamond configuration we create pairs where one photon is at 780 nm and the other is at 1367 nm. Other choices of the upper state in the diamond can result in photons at 1550 nm which is currently the prime telecommunications wavelength. We are able to show that temporal profile of the biphotons is for a large part dominated by the linear absorption of the 780 nm photons. Modifying absorption by changing the pump laser parameters, or by adding another control laser, changes both the temporal and spectral properties of the pairs.

We were able to test fundamental quantum mechanical predictions and as expected quantum mechanics won out. The tests include Bell's inequality violation, which definitively shows that the pairs produced are polarization entangled. The measured polarization state is consistent with a simplified model that takes into account all the relevant rubidium level structure. We show that the biphoton light field violates the Cauchy-Shwarz inequality convincingly, further demonstrating its non-classical nature. We also show the indivisibility of the photon and look at the photon pairs as a source of narrow bandwidth, high spectral brightness, heralded single photons.

In the introduction we looked at the advantages of a telecom quantum repeater for entanglement distribution. The question still stands whether the photons produced by our system could be used for such an application. To answer that question the system should be examined in the pulsed pump regime. We can, however, use our results from continuously pumped experiments as a guide. We saw that in the off resonantly pumped case that the photon pairs had bandwidths on the order of 350 MHz. This makes storage difficult when the natural linewidth of the pertinent atomic transitions is 6 MHz. In the resonantly pumped case the photon pairs have a much narrower linewidth, as low as 15 MHz. This improvement came with a large uncorrelated background. Also, the existence of quantum beats means the photons are split between two wavelengths separated by the hyperfine splitting but this was remedied by including a control laser to decouple one of the intermediate states. This thesis has shown the mechanisms available for control of the spectral and temporal characteristics of the biphoton. Those tools and others, such as EIT, may help overcome the largest limiting factor in the system, the linear absorption through the medium. Electromagnetically induced transparency could potentially provide a great increase in the generation rate and a reduction in the linewidth of the generated pairs. A Λ-scheme EIT could provide a narrow highly transparent window with the complication that the EIT control laser will necessarily be nearly degenerate with the created photon. A cascade EIT structure could circumvent this difficulty but high transparency in the cascade configuration is more difficult to achieve.

Bibliography

[1] A Aspect, J Dalibard, P Grangier, and G Roger. Quantum beats in continuously excited atomic cascades. *Opt. Comm.*, 49:429, 1984.

[2] A. Aspect, P. Grangier, and G. Roger. Experimental tests of realistics local theories via bell's theorem. *Phys. Rev. Lett.*, 47:460, 1981.

[3] S. H. Autler and C. H. Townes. Stark effect in rapidly varying fields. *Phys. Rev.*, 100:703, 1955.

[4] Vlatko Balic, Danielle A. Braje, Pavel Kolchin, G.Y. Yin, and S. E. Haris. Generation of paired photons with controllable waveforms. *Phys. Rev. Lett.*, 94:183601, 2005.

[5] F. E. Becerra, R. T. Willis, S. L. Rolston, and L. A. Orozco. Nondegenerate four-wave mixing in rubidium vapor: The diamond configuration. *Phys. Rev. A*, 78:013834, 2008.

[6] J S Bell. On the einstein-rosen-podolsky paradox. *Physics*, 1(195), 1965.

[7] C. H. Bennett and G. Brassard. Quantum cryptography: Public key distribution and coin tossing. *Proceedings of the IEEE International Conference on Computers, Systems and Signal Processing, Ba*, page 175, 1984.

[8] E D Black. An introduction to pound-drever-hall laser frequency stabilization. *Am. J. Phys.*, 69:79, 2001.

[9] Robert W. Boyd. *Nonlinear Optics*. Academic Press, 2003.

[10] Robert W. Boyd, Michelle S. Malcuit, and Daniel J. Gauthier. Competition between amplified spontaneous emission and the four-wave-mixing process. *Phys. Rev. A*, 35:1648, 1987.

[11] V. Boyer, A M Marino, R C Pooser, and P D Lett. Entangled images from four-wave mixing. *Science*, 321:544, 2008.

[12] V. Boyer, A.M. Marino, and P.D. Lett. Generation of spatially broadband twin beams for quantum imaging. *Phys. Rev. Lett.*, 100:143601, 2008.

[13] H J Briegel, W Dür, J I Cirac, and P Zoller. Quantum repeaters: The role of imperfect local operatons in quantum communication. *Phys. Rev. Lett.*, 81:5932, 1998.

[14] H J Carmichael. *Statistical Methods in Quantum Optics 1: Master Equations and Fokker-Planck Equations*. Springer-Verlag, Berlin, 1999.

[15] H. J. Carmichael. *Statistical Methods in Quantum Optics 2: Non-Classical Fields*. Springer, Berlin, 2008.

[16] T. Chaneliere, D. N. Matsukevich, S. D. Jenkins, S.-Y. Lan, T. A. B. Kennedy, and A. Kuzmich. Storage and retrieval of single photons transmitted between remote quantum memories. *Nature*, 438:833, 2005.

[17] T. Chaneliere, D.N. Matsukevich, S.D. Jenkins, T.A.B. Kennedy, M.S. Chapman, and A. Kuzmich. Quantum telecommunications based on atomic cascade transitions. *Phys. Rev. Let.*, 96:093604, 2006.

[18] Q.-F. Chen, B.-S. Shi, M. Feng, Y.-S. Zhang, and G.-C. Guo. Non-degenerate nonclassical photon pairs in a hot atomic ensemble. *Opt. Exp.*, 16:21708, 2008.

[19] C-W Chou, J Laurat, H Deng, K S Choi, H de Riedmatten, D Felinto, and H J Kimble. Functional quantum nodes for entanglement distribution over scalable quantum networks. *Science*, 316:1316, 2007.

[20] J. F. Clauser, M. A. Horne, A. Shimony, and R. A. Holt. Proposed experiment to test local hidden-varible theories. *Phys. Rev. Lett.*, 23:880, 1969.

[21] K L Corwin, Z T Lu, C F Hand, R J Epstein, and C E Wieman. Frequency-stabilized diode laser with the zeeman shift in an atomic vapor. *Appl. Opt.*, 37:3295, 1998.

[22] L. Deng, M. Kozuma, E. W. Hagley, and M. G. Payne. Opening optical four-wave mixing channels with giant enhancement using ultraslow pump waves. *Phys. Rev. Lett.*, 88:143902, 2002.

[23] R W P Drever, J L Hall, F B Kowalsky, J Hough, G M Ford, A J munley, and H Ward. Laser phase and frequency stabilization using an optical resonator. *Appl. Phys. Lett.*, 31:97, 1983.

[24] Shengwag Du, Chinmay Belthangady, Pavel Kolchin, G. Y. Yin, and S.E. Harris. Observation of optical precursors at the biphoton level. *Opt. Lett.*, 33(18):2149, 2008.

[25] Shengwag Du, Pavel Kolchin, Chinmay Bethangady, G.Y. Yin, and S. E. Harris. Generation of paired photons with controllable waveforms. *Phys. Rev. Lett.*, 100:183603, 2008.

[26] L.M. Duan, M.D. Lukin, J.I. Cirac, and P. Zoller. Long-distance quantum communication with atomic ensembles and linear optics. *Nature*, 414:413, 2001.

[27] Oughstun K. E. and Sherman G. C. *Pulse Propagation in Causal Dielectrics*. Springer-Verlag, 1994.

[28] J. H. Eberly and K. Wókdiewicz. The time-dependent physical spectrum of light. *J. Opt. Soc. Am.*, 69(9):1252, 1977.

[29] A Einstein, B Podolsky, and N Rosen. Can a quantum-mechanical description of reality be considered complete? *Phys. Rev.*, 47:777, 1935.

[30] S J Freedman and J F Clauser. Experimental test of local hidden-variable theories. *Phys. Rev. Lett.*, 28:938, 1972.

[31] N. Gisin, G. Ribordy, W. Tittel, and H. Zbinden. Quantum cryptography. *Rev. Mod. Phys.*, 74:145, 2002.

[32] E. A. Goldschmidt, M. D. Eisaman, J. Fan, S. V. Polyakov, and A. Migdall. Spectrally bright and broad fiber-based heralded single-photon source. *Phys. Rev. A*, 78:013844, 2008.

[33] P Grangier, G Roger, A Aspect, A Heidmann, and S Reynaud. Observation of photon antibunching in phase-matched multiatom resonance fluorescence. *Phys. Rev. Lett.*, 57:687, 1986.

[34] Heejeong Jeong, Andrew M. C. Dawes, and Daniel J. Gauthier. Direct observation of optical precursors in a region of anomalous dispersion. *Phys. Rev. Lett.*, 96:143901, 2006.

[35] E Knill, R Laflamme, and G J Milburn. A scheme for efficient quantum computation with linear optics. *Nature*, 409:46, 2001.

[36] Pavel Kolchin. Electromagnetically-induced-transparency-based paired photon generation. *Phys. Rev. A*, 75:033814, 2007.

[37] A Kuzmich, W P Bowen, A D Booze, A Boca, C W Chou, and L-M Duan adn H J Kimble. Generation of nonclassical photon pairs for scalable quantum communication with atomic ensembles. *Nature*, 423:731, 2003.

[38] P. G. Kwiat, K. Mattle, H. Weinfurter, A. Zeilinger, A. V. Sergienko, and Y. Shih. New high-intensity source of polarization-entangled photon pairs. *Phys. Rev. Lett.*, 75:4337, 1995.

[39] X. Li, P. L. Voss, J. E. Sharping, and P. Kumar. Optical-fiber source of polarization-entangled photons in the 1550 nm telecom band. *Phys. Rev. Lett.*, 94:053601, 2005.

[40] M. D. Lukin and A. Imamoglu. Nonlinear optics and quantum entanglement of ultraslow single photons. *Phys. Rev. Lett.*, 84(7):1419, 2000.

[41] Leonard Mandel and Emil Wolf. *Optical Coherence and Quantum Optics*. Cambridge University Press, New York, 1995.

[42] A. M. Marino, V. Boyer, and P. D. Lett. Violation of the cauchy-schwarz inequality in the macroscopic regime. *Physical Review Letters*, 100(23):233601, 2008.

[43] D N Matsukevich, P Maunz, D L Moehring, S Olmschenk, and C Monroe. Bell inequality violation with two remote atomic qubits. *Phys. Rev. Lett.*, 100:150404, 2008.

[44] P. D. McDowall and M F Andersen. Acousto-optic modulator based frequency stabilized diode laser system for atom trapping. *Rev. Sci. Instr.*, 80:053101, 2009.

[45] A. R. McMillan, J. Fulconis, M. Halder, C. Xiong, J. G. Rarity, and W. J. Wadsworth. Narrowband high-fidelity all-fibre source of heralded single photons at 1570 nm. *Opt. Exp.*, 17:6156, 2009.

[46] H J Metcalf and P Straten. *Laser Cooling and Trapping*. Springer, New York, 1999.

[47] A. F. Molisch and B. P. Oehry. *Radiation Trapping in Atomic Vapours*. Oxford University Press, 1998.

[48] B R Mollow. Power spectrum of light scattered by two-level systems. *Phys. Rev.*, 188:1969, 1969.

[49] Giovanna Morigi, Sonja Franke-Arnold, and Gian-Luca Oppo. Phase-dependent interaction in a four-level atomic configuration. *Phys. Rev. A*, 66:053409, 2002.

[50] J. S. Neergaard-Nielsen, B. M. Nielsen, H. Takahashi, A. I. Vistnes, and E. S. Polzik. High purity bright single photon source. *Opt. Express*, 15(13):7940–7949, 2007.

[51] T Okoshi, K Kikuchi, and A Nakayama. Novel method for high resolution measurement of laser output spectrum. *Electronics Letters*, 16(16):630, 1980.

[52] Z. Y. Ou and L. Mandel. Violation of bell's inequality and classical probability in a two-photon correlation experiment. *Phys. Rev. Lett.*, 61(1):50–53, Jul 1988.

[53] S. V. Polyakov, C. W. Chou, D. Felinto, and H. J. Kimble. Temporal dynamics of photon pairs generated by an atomic ensemble. *Phys. Rev. Lett.*, 93:263601, 2004.

[54] M. D. Reid and D. F. Walls. Violations of classical inequalities in quantum optics. *Phys. Rev. A*, 34:1260, 1986.

[55] Danna Rosenberg, Adriana E. Lita, Aaron J. Miller, and Sae Woo Nam. Noise-freee high-efficiency photon-number-resolving detectors. *Phys. Rev. A*, 71:061803(R), 2005.

[56] U. Schnorrberger, J. D. Thompson, S. Trotzky, R. Pugatch, N. Davidson, S. Kuhr, and I. Bloch. Electromagnetically induced transparency and light storage in an atomic mott insulator. *Physical Review Letters*, 103(3):033003, 2009.

[57] Marlan O. Scully and M. Suhail Zubairy. *Quantum Optics*. Cambridge University Press, 1997.

[58] Y. H. Shih and C. O. Alley. New type of einstein-podolsky-rosen-bohm experiment using pairs of light quanta produced by optical parametric down conversion. *Phys. Rev. Lett.*, 61(26):2921, Dec 1988.

[59] R E Slusher, L W Hollberg, B Yurke, J C Mertz, and J. F. Valley. Observation of squeezed states generated by four-wave mixing in an optical cavity. *Phys. Rev. Lett.*, 55:2409, 1985.

[60] C. H. van der Wal, M. D. Eisaman, A. Andre, R. L. Walsworth, D. F. Phillips, A. S. Zibrov, and M. D. Lukin. Atomic memory for correlated photon states. *Science*, 301:196, 2003.

[61] R. T. Willis, F. E. Becerra, L. A. Orozco, and S. L. Rolston. Four-wave mixing in the diamond configuration in an atomic vapor. *Phys. Rev. A*, 79:033814, 2009.

[62] W K Wootters and W. H. Zurek. A single quantum cannot be cloned. *Nature*, 299:802, 1982.

[63] Z-S Yuan, Y-A Chen, B Zhao, S. Chen, J. Schmiedmayer, and J-W Pan. Experimental demonstration of a bdcz quantum repeater node. *Nature*, 454:1098, 2008.

[64] R. Zhao, Y. O. Dudin, S. D. Jenkins, C. J. Campbell, D. N. Matsukevich, T. A. B. Kennedy, and A. Kuzmich. Long-lived quantum memory. *Nature Phys.*, 5:100, 2009.

[65] W Z Zhao, J E Simsarian, L A Orozco, and G D Sprouse. A computer-based digital feedback control of frequency drift of multiple lasers. *Rev. Sci. Instrum.*, 69:3737, 1998.